

# Thermal-infrared imaging of 3C radio galaxies at $z \sim 1$

Chris Simpson,<sup>1</sup> Steve Rawlings<sup>2</sup> and Mark Lacy<sup>2</sup>

<sup>1</sup>*Subaru Telescope, National Astronomical Observatory of Japan, 650 N. A'Ohōkū Place, Hilo, HI 96720, U.S.A.*

<sup>2</sup>*Astrophysics, Department of Physics University of Oxford, Keble Road, Oxford OX1 3RH*

18 June 2018

## ABSTRACT

We present the results of a programme of thermal-infrared imaging of nineteen  $z \sim 1$  radio galaxies from the 3CR and 3CRR (LRL) samples. We detect emission at  $L'$  ( $3.8\mu\text{m}$ ) from four objects; in each case the emission is unresolved at 1-arcsec resolution. Fifteen radio galaxies remain undetected to sensitive limits of  $L' \approx 15.5$ . Using these data in tandem with archived *HST* data and near-infrared spectroscopy we show that three of the detected ‘radio galaxies’ (3C 22, 3C 41, and 3C 65) harbour quasars reddened by  $A_V \lesssim 5$ . Correcting for this reddening 3C 22 and 3C 41 are very similar to coeval 3C quasars, whilst 3C 65 seems unusually underluminous. The fourth radio galaxy detection (3C 265) is a more highly obscured ( $A_V \sim 15$ ) but otherwise typical quasar which previously has been evident only in scattered light. We determine the fraction of dust-reddened quasars at  $z \sim 1$  to be  $28^{+23}_{-13}\%$  at 90% confidence. On the assumption that the undetected radio galaxies harbour quasars similar to those in 3C 22, 3C 41 and 3C 265 (as seems reasonable given their similar narrow emission line luminosities) we deduce extinctions of  $A_V \gtrsim 15$  towards their nuclei. The contributions of reddened quasar nuclei to the total  $K$ -band light ranges from  $\sim 0$  per cent for the non-detections, through  $\sim 10$  per cent for 3C 265 to  $\sim 80$  per cent for 3C 22 and 3C 41. Correcting for these effects does not remove the previously reported differences between the  $K$  magnitudes of 3C and 6C radio galaxies, so contamination by reddened quasar nuclei is not a serious problem for drawing cosmological conclusions from the  $K$ - $z$  relation for radio galaxies. We discuss these results in the context of the ‘receding torus’ model which predicts a small fraction of lightly-reddened quasars in samples of high radio luminosity sources. We also examine the likely future importance of thermal-infrared imaging in the study of distant powerful radio sources.

**Key words:** galaxies: active – galaxies: nuclei – galaxies: photometry – infrared: galaxies – radio continuum: galaxies

## 1 INTRODUCTION

Luminous extragalactic radio sources are associated with either quasars or radio galaxies, the latter class of object lacking the bright non-stellar continuum and prominent broad emission lines that characterize the former. For many years astronomers have speculated that at least some radio galaxies harbour an active nucleus which, although obscured from view along the line of sight, would be observed as a quasar if seen from certain other, favourable directions (e.g., Scheuer 1987). There is now overwhelming observational evidence that this is the case. Most notably, spectropolarimetry has revealed the presence of quasar-like broad emission lines in the polarized flux spectra of a number of radio galaxies (e.g., Tran et al. 1998 and references therein). In such cases the broad lines are hidden from direct view but are scattered into our line of sight by a screen of either dust or electrons. However, the more general proposition that *all* radio galax-

ies harbour obscured quasar nuclei has not yet been confirmed.

It is generally believed that the unobscured lines of sight lie close to the axis of the twin radio jets, and that quasars are therefore seen more nearly ‘pole-on’ than their radio galaxy counterparts (e.g., Barthel 1989). This is supported by the presence of bright radio cores and one-sided jets in quasars that are weak or absent in radio galaxies (e.g., Owen & Puschell 1984), a result which is most naturally explained by Doppler boosting of emission from relativistic jets moving close to the line of sight. Even more compelling evidence comes from optical polarization studies that have revealed many radio galaxies in which the rest-frame ultraviolet light is strongly polarized with its electric vector lying perpendicular to the radio axis (e.g., Tadhunter et al. 1992). These observations suggest that quasar light can emerge relatively unhindered along the radio axis, and reach the observer after scattering, whilst direct transmitted radiation from the quasar nucleus is effectively blocked. Such processes are also

at least partly responsible for the so-called ‘alignment effect’ (Chambers, Miley & van Breugel 1987; McCarthy et al. 1987) — the tendency for the elongation of optical and radio structures along a common axis.

In an orientation-based unification scheme such as this, the obscuring material lies preferentially in the plane perpendicular to the radio jets, and a central parameter is the angle between the radio axis and the line of sight which grazes the edge of the obscuring material (generally referred to as the ‘torus’). A simple model which is often considered relates this critical angle  $\theta_c$  to the inner radius of the torus,  $r$ , and its half-height,  $h$ , via  $\tan \theta_c = r/h$  (see, e.g., Simpson 1998). In this model there are physical reasons why  $r$ , and hence  $\theta_c$ , might be expected to correlate with quasar luminosity: if the value of  $r$  is determined by the radius at which dust sublimates in the radiation field of the quasar then it should increase with the photoionizing luminosity of the quasar as  $L_{\text{phot}}^{0.5}$  (Lawrence 1991). This picture where the torus opens up as the luminosity of the quasar increases is known as the ‘receding torus’ model. Strong links between the intrinsic UV/optical luminosity of the quasar nuclei of radio sources and extended radio luminosity are now firmly established (Rawlings & Saunders 1991; Falcke, Malkan & Biermann 1995; Serjeant et al. 1998; Willott et al. 1998c) in the sense that  $L_{\text{phot}} \propto L_{178}^{0.6}$  where  $L_{178}$  is the 178-MHz (extended) radio luminosity. It therefore seems highly plausible that  $r$  and hence  $\theta_c$  will rise, albeit slowly, with radio luminosity ( $\tan \theta_c \propto L_{178}^{0.3}$ ),

The brightest (3C) radio sources at  $z \sim 1$  are about 100 times more radio luminous than 3C sources at  $z \sim 0.1$ , so assuming  $h$  to be independent of  $L_{178}$  and  $z$ , we expect  $r$  and hence  $\tan \theta_c$  to be a factor  $\sim 4$  greater for these objects. The quasar fraction should therefore be correspondingly larger, and, since lines of sight grazing the torus will subtend a much lower solid angle, the fraction of lightly-reddened quasars should be much reduced (see Hill et al. 1996). Based on their detection of a high fraction of lightly-reddened quasar nuclei from near-infrared spectroscopy of Pa $\alpha$  in low-redshift ( $0.1 \leq z < 0.2$ ) 3C radio sources, Hill, Goodrich & DePoy (1996) found  $\theta_c \approx 20^\circ$ , and used the receding torus model to make quantitative predictions about the distribution of nuclear extinctions in higher-redshift, more radio luminous, sources. Their predictions were in rough agreement with Economou et al.’s (1995) discovery of only one broad H $\alpha$  line in a preliminary analysis of a sample of ten radio galaxies at  $z \sim 1$ . However, as Rawlings et al. (1995) discuss, spectroscopic methods of detecting hidden quasar nuclei lack the sensitivity to provide a good general method of characterizing the angular distribution of reddening towards quasar nuclei in radio galaxies at  $z \sim 1$ . This is because of the large optical depth expected towards rest-frame optical lines like H $\alpha$ , and the poor sensitivity to weak rest-frame near-infrared lines like Pa $\alpha$ , particularly once they become redshifted beyond the  $K$ -band (at  $z > 0.3$  in the case of Pa $\alpha$ ). A definitive test of the receding torus model for high-redshift objects has therefore yet to be performed.

The distribution of reddenings to the quasar nuclei may also have important cosmological implications, since the near-infrared Hubble diagram for radio galaxies (Fig. 1) — and the common assumption that the near-infrared emission of radio galaxies is dominated by starlight — has been used to infer constraints on the formation and evolution of ellipti-

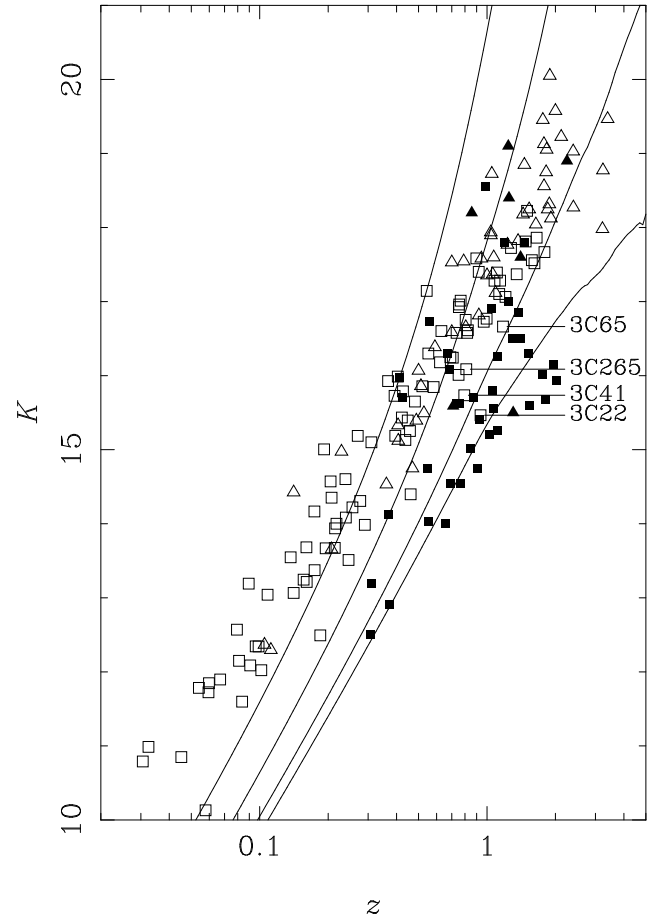


**Figure 1.** The near-infrared Hubble Diagram for radio sources. The objects are taken from the 3CRR (LRL) sample (squares; Laing, Riley & Longair 1983), and the 6C sample (triangles; Eales 1985, slightly revised by Rawlings et al. 1998b); quasars are represented by filled symbols, and other objects by open symbols. We define quasars as having a nuclear point source with  $M_B < -23$ ; with this criterion, all quasars display broad optical emission lines, but some of the other objects, which we term radio galaxies, also display broad lines, either weakly or in polarized flux only.  $K$ -band photometry for the LRL sample has been taken from Best et al. (1998), Lilly & Longair (1982, 1984), Lilly, Longair & Miller (1985) and Rawlings et al. (1995). Although 73 of the 94  $z > 0.1$  LRL radio galaxies have  $K$ -band photometry (and in all but one case the lack of  $K$ -band data stems from the inability to observe high-declination objects at UKIRT), almost all the quasars lack such data; to plot the quasars we have estimated  $K$ -band magnitudes using optical photometry from LRL, and an extrapolation based on the canonical quasar spectrum described in Section 1. Note that contributions from the host galaxies of quasars, and the possibility of their suffering significant reddening mean that these estimated  $K$  values should be treated as upper limits.  $K$ -band photometry and redshifts for 6C sources are from Eales et al. (1997) and Rawlings et al. (1998b) respectively. 39 of the 41  $z > 0.1$  6C radio galaxies in the 6C sample have  $K$ -band photometry; we again estimate  $K$ -band magnitudes for the 7 quasars using optical photometry (Eales 1985) and the canonical quasar spectrum. The lines show the loci of a model quasar with  $M_B = -26$  reddened by  $A_V = 0, 2, 7, 15$ ; the lowest curve is for  $A_V = 0$ , increasingly higher curves represent increasing values of  $A_V$ . A few objects of special interest are labelled.

cal galaxies (e.g., Lilly 1989; Eales et al. 1993). The discovery that the  $K$ -band magnitudes of 6C radio galaxies, i.e., those selected at a  $\sim 6$  times lower radio flux limit than 3C, are  $\sim 0.6$  magnitudes fainter than those of 3C radio galaxies at the same redshift (Eales et al. 1997) suggests that there is some close link between radio luminosity and near-infrared luminosity. Either, stellar luminosity — and by inference stellar mass — correlates with radio luminosity, or there is some important component of the near-infrared luminosity which can be ascribed to a hidden quasar nucleus. Recent discussions of these possibilities can be found in Eales et al. (1997), Best, Longair & Röttgering (1998) and Roche, Eales & Rawlings (1998). Although there is direct observational evidence from near-infrared polarimetry (Leyshon & Eales 1998) that scattered light makes only a small (few per cent) contribution to the near-infrared luminosity of radio galaxies even when it makes a very significant contribution in the ultraviolet and optical, it has not yet been conclusively shown that reddened quasar light is also a negligible component. As illustrated by Fig. 1, such quasar nuclei would need to be subject to only a fairly limited amount of reddening ( $A_V \sim 2$ – $7$ ) in order not to possess obvious quasar features in their optical spectra whilst still contributing to the  $K$ -band luminosity at the level of radio galaxies lying close to the mean  $K$ - $z$  relation for radio galaxies. The existence of a substantial population of moderately-reddened quasars has been suggested by Webster et al. (1995), although both the reality and importance of this population have been questioned (Serjeant & Rawlings 1996; Benn et al. 1998).

In this paper we report on the results from a project designed with two principal aims. The first aim was to determine the contribution of transmitted quasar light to the  $K$ - $z$  relation for  $z \sim 1$  radio galaxies, and hence determined whether reddened quasar nuclei can explain the difference in near-infrared luminosities between 3C and 6C radio galaxies. The second aim was to constrain the range of  $A_V$  towards the quasar nuclei of luminous radio sources at  $z \sim 1$ , and to compare this range with the predictions of the receding torus model. The project was based around thermal-infrared imaging since, as discussed by Rawlings et al. (1995) this is for these purposes a much more powerful technique than spectroscopy. Its utility rests on the dramatic divergence of the rest-frame spectral energy distributions (SEDs) of starlight and quasar light redward of  $1 \mu\text{m}$  (see Fig. 2).

Although there is considerable variation in the quantitative spectral energy distributions of quasars, the inflexion at  $1 \mu\text{m}$  appears to be a universal feature (Neugebauer et al. 1987; Sanders et al. 1989; Elvis et al. 1994), except for blazar-type sources where synchrotron emission dominates even at optical-infrared wavelengths. The rise to longer wavelengths is believed to be due to dust at or near its sublimation temperature ( $T \sim 1500 \text{ K}$ ). Kobayashi et al. (1993) have successfully modelled the near-infrared continua of low-redshift quasars in this manner, and Barvainis (1987) has shown that the entire infrared spectrum from  $1$ – $100 \mu\text{m}$  can be attributed to dust at a range of temperatures, with the hottest dust contributing most strongly at the shortest wavelengths. If the dust is heated by, and in thermal equilibrium with, the radiation field of the quasar, then the hottest dust must originate close to the central engine. Thus even though emission from the hot dust may be optically thin and hence isotropic, it could easily be occluded by the larger-scale ob-

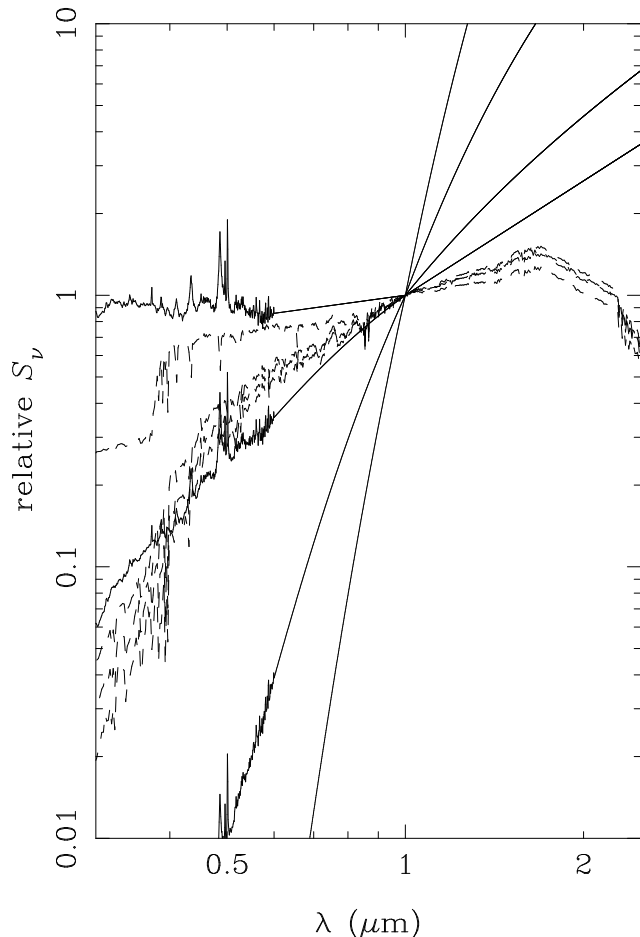


**Figure 2.** Comparison of the spectral energy distributions SEDs of stellar populations (of various ages) and quasars (subject to various amounts of reddening). Stellar population loci (dashed curves) are 1-Gyr bursts at ages 1, 2, 3, and 5 Gyr (younger ages correspond to bluer colours) from the GISSEL96 models (Bruzual & Charlot 1993, 1998). Quasar loci (full lines) have been calculated using the canonical spectrum described in Section 1 as seen through 0.2, 7, and 15 mag of visual extinction in the rest-frame of the quasar host galaxy (lower extinctions correspond to bluer colours). All the SEDs have been normalized at  $1 \mu\text{m}$ . Note the similarities between the SEDs of lightly-reddened quasars ( $A_V \sim 2$ ) and old stellar populations blueward of  $1 \mu\text{m}$ , but the divergence at longer wavelengths.

scuring material so that the emergent flux becomes a strong function of viewing angle. The attenuation suffered at angles greater than  $\theta_c$  should, however, be much less severe than at shorter wavelengths. The apparent constancy of the near-infrared continuum slope in quasars (Neugebauer et al. 1987), and the possibility that the emitting regions are optically thin makes it an ideal region of the spectrum from which to determine the reddening.

The structure of this paper is as follows. In Section 2 we describe our selection of targets for thermal-infrared imaging. In Section 3 we describe our new imaging observations with the 3.9-m United Kingdom Infrared Telescope (UKIRT). In Section 4 we present the results of these observations and our analysis of the data. In Section 5 we widen our analysis to include archival data from the Hubble Space

Telescope (*HST*), as well as a new near-infrared spectrum obtained at UKIRT. In Section 6 we discuss the implications of our results, including both a discussion of the effects of hidden quasar nuclei on the  $K$ - $z$  relation and a test of the receding torus model. In Section 7 we review the prospects for future observations of the type discussed in this paper.

Throughout this paper we have assumed  $H_0 = 50 \text{ km s}^{-1} \text{ Mpc}^{-1}$ ,  $q_0 = 0.5$  and  $\Lambda = 0$ . The convention for spectral index,  $\alpha$ , is that  $S_\nu \propto \nu^{-\alpha}$ , where  $S_\nu$  is the flux density at frequency  $\nu$ . We have adopted a canonical rest-frame spectrum for a quasar of the following form: the composite quasar spectrum from Francis et al. (1991) for wavelengths from  $0.1$ – $0.6 \mu\text{m}$ , a power law with  $\alpha = 0.3$  from  $0.6$ – $1 \mu\text{m}$ , and a power law with  $\alpha = 1.4$  from  $1$ – $3 \mu\text{m}$ . The motivation for the broken power-law form at near-IR wavelengths is provided by the data of Neugebauer et al. (1987). We adopt the empirical extinction curve for the Milky Way given by Pei (1992) as our assumed dust extinction curve.

## 2 SELECTION OF TARGETS

Our primary goal in this project was to study a complete subsample of radio galaxies from the 3CRR sample — which we hereafter refer to as the LRL sample (after Laing, Riley & Longair 1983) in order to more easily differentiate it from the 3CR sample — in the redshift range  $0.65 \leq z < 1.20$ . These objects have 178-MHz radio luminosities  $L_{178} > 10^{27} \text{ W Hz}^{-1} \text{ sr}^{-1}$ , and they lie at redshifts where  $3.8 \mu\text{m}$  imaging probes rest-frame wavelengths in the region of primary interest (see Fig. 2). However, a combination of scheduling, technical problems, and poor weather meant that we were often either unable to observe all the sources within a given patch of sky, or conversely were short of targets. In the former case, we chose the targets to observe based solely on position in the sky so as to make our observing programme as efficient as possible, while in the latter case, we supplemented our list from the 3CR catalogue of Bennett (1962a,b), on which LRL is based. The declination limit of UKIRT forced us to exclude targets with  $\delta > +60^\circ$ . Over the course of the three observing runs assigned to this project, plus some additional spare time on three other nights, we were able to observe all twelve radio galaxies from 3CR and LRL satisfying  $\alpha > 16^{\text{h}}$  and  $\alpha < 04^{\text{h}}20^{\text{m}}$ . Our coverage in the RA range  $09^{\text{h}} < \alpha < 14^{\text{h}}$  is less complete. We observed a randomly-selected subsample of five 3C radio galaxies from the eight with  $0.8 < z < 1.0$ ; the excluded sources were 3C 237 (in 3CR only) and 3C 263.1 and 3C 280 (also in LRL). We provide relevant data for our 3CR (but non-LRL) targets in Table 1; a useful recent reference for data on the LRL sample is Blundell et al. (1998). A full list of our targets is included in Table 2

In Fig. 3, we compare the location of our UKIRT targets with the full LRL sample in a plot of radio core luminosity versus redshift. This figure introduces two new classes containing objects traditionally classified as radio galaxies (e.g., in LRL) but with broad emission lines in their optical and/or near-infrared spectra. The first new class accounts for objects with prominent broad lines in their direct-light spectra but nuclear optical continuum luminosities below the  $M_B = -23$  limit often taken as the minimum required for a quasar (hereafter class-‘B’ radio galaxies; see Willott et

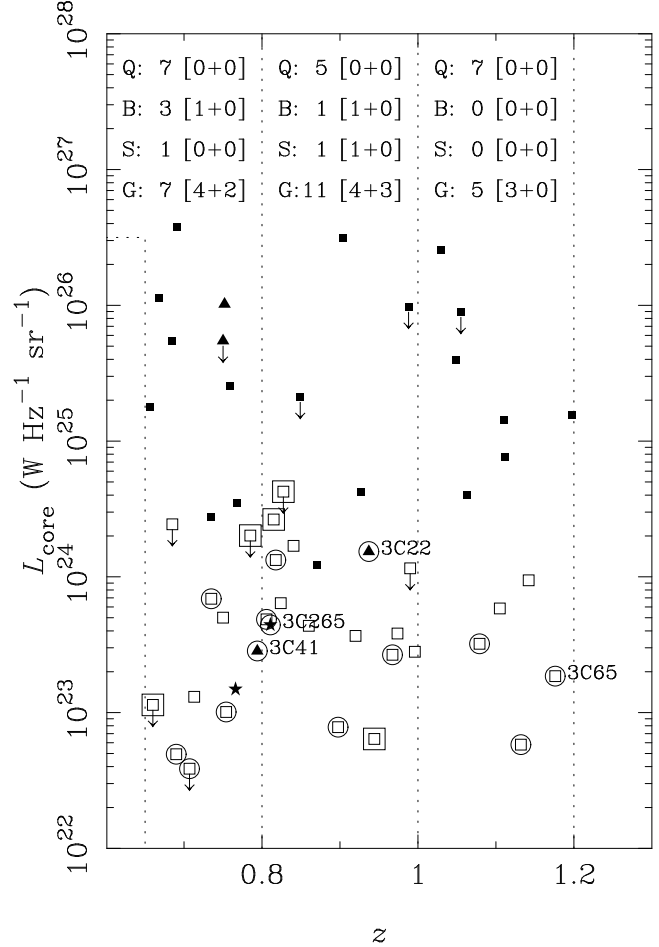


**Figure 3.** Radio core luminosity (evaluated at or near 5 GHz) versus redshift for all objects from the LRL sample with  $0.65 \leq z < 1.20$  plus additional UKIRT targets. UKIRT targets are indicated by large symbols: large circles denoting LRL objects; and large squares, objects which are only in 3CR. The smaller symbols have meanings as follows: filled squares represent quasars (class ‘Q’); filled triangles, radio galaxies with broad lines prominent in direct-light spectra (‘B’); filled stars, radio galaxies with broad lines seen only because of a large scattered (polarized) component (‘S’); and open squares, narrow-line radio galaxies (‘G’). The numbers in each category in each of three marked redshift bins are summarized at the top of the plot, with the first number relating to the total number in LRL, the second to the number of LRL objects observed with the UKIRT, and the third number to the 3CR (only) UKIRT targets. A few objects of special interest are labelled.

al. 1998b for further discussion). Since these criteria ignore any reddening corrections, class-‘B’ radio galaxies include both lightly-reddened quasars and those that are simply intrinsically weak. The second class accounts for objects with broad emission lines which are prominent only in scattered light as evidenced by spectropolarimetric observations (hereafter class-‘S’ radio galaxies; e.g., Tran et al. 1998). Class-‘S’ objects obviously harbour quasar nuclei, but according to unified schemes may be being observed very far from a pole-on orientation. Fig. 3 illustrates the dichotomy between the radio core properties of quasars and narrow-line radio

**Table 1.** Relevant data on the UKIRT 3CR targets which are not in the LRL sample. Positions are either optical (from McCarthy et al. 1997) or radio (from Strom et al. 1990). We provide radio core measurements (and the frequency at which these measurements were made) and the largest (projected) angular sizes of the radio sources from the following references: B94, Bogers et al. (1994); L75, Longair (1975); R96, Rhee et al. (1996); S90, Strom et al. (1990).

Name	Pos	$\alpha$ (B1950)	$\delta$	$S_{\text{core}}$ (mJy)	$\nu$ (GHz)	LAS (")	Ref
3C 44	O*	01 28 45.12	+06 08 17.7	< 1.0	8.0	65	B94
3C 54	O	01 52 25.91	+43 31 20.9	< 25.0	5.0	54	L75
3C 107	O	04 09 49.88	−01 07 10.6	< 13.0	1.4	13	R96
3C 114	R	04 17 29.05	+17 46 49.0	16.0	5.0	54	S90
3C 272	R	12 22 00.81	+42 23 12.3	0.3	5.0	59	S90

\*Position estimated from the countour plot in McCarthy et al. (1997) since the position given in their Table 3 is incorrect.

galaxies and hints that class-‘B’ (and maybe class-‘S’) radio galaxies are intermediary cases.

We next consider possible biases introduced by our incomplete UKIRT observational programme. The summary numbers included in Fig. 3 show that we have obtained UKIRT data for about half of the possible target LRL radio galaxies with no significant redshift bias across the full range. There are insufficient data to consider any more than one redshift bin in our later analysis, but we note that on the basis of Fig. 3 there is very little evidence for any change in quasar fraction with redshift across this bin (although see Lawrence 1991). Again because of lack of data we are forced to include the non-LRL objects in our analysis without considering them separately from the LRL objects. There is some worry that this might introduce a small bias because these objects were typically excluded from LRL because their accurate radio flux densities fall slightly below the LRL limit, and as discussed in Section 1 their lower radio luminosities might be expected to translate into lower quasar luminosities. To assess the impact of this effect we plot in Fig. 4 the [O II] narrow-line luminosity,  $L_{[\text{O II}]}$ , versus 178-MHz radio luminosity,  $L_{178}$ , for the parent LRL sample plus our additional UKIRT targets. This plot is relevant because according to unified schemes the [O II] luminosity should be much more closely related to the underlying quasar luminosity than  $L_{178}$  (e.g., Hes, Barthel & Fosbury 1993). Although Simpson (1998) has suggested that the optical [O III] doublet provides a more reliable probe of the intrinsic quasar luminosity, the wavelengths to which these lines are redshifted for sources in our sample mean there exist very few measurements of their strengths. The effects of using different narrow lines are subtle compared to the points we shall make on the basis of Fig. 4. Any correlation in Fig. 4 is much weaker than the one seen when objects spanning several orders of magnitude in  $L_{178}$  are plotted (e.g., Willott et al. 1998c). This demonstrates that the scatter in the  $L_{[\text{O II}]}$ ,  $L_{178}$  relation is sufficiently large that the factor  $\sim 2$  difference in  $L_{178}$  between the 3CR and LRL objects has negligible effect on the expected difference in underlying quasar luminosities. Kolmogorov–Smirnov tests show that the distribution of  $L_{[\text{O II}]}$  for the UKIRT targets is indistinguishable from that for the unobserved LRL galaxies alone, and from that for the unobserved LRL galaxies and quasars combined. The lower scatter displayed in  $L_{[\text{O II}]}$  by the quasars is at least in part due to that fact that for a significant number of them (7/19) we have inferred the line luminosity from broad-band photometry by assuming a single rest-frame equivalent width, whereas in reality there is

a significant spread in this property. We conclude, and shall assume hereafter, that our UKIRT targets form an unbiased selection of 3C radio galaxies in the target redshift range.

In Section 6 we will need to consider an unbiased sample of radio sources including both quasars and radio galaxies. To do this we must estimate the number of quasars which would exist in a sample with the same incomplete selection criteria as our radio galaxy sample. Excluding 3C 454.3, whose presence in LRL is due to Doppler-boosted core emission leaves 19 LRL quasars with  $0.65 \leq z < 1.20$ , compared to 29 galaxies. This quasar fraction (40 per cent) corresponds to a torus opening angle  $\theta_c = 53^\circ$ . Our sample of 19 radio galaxies observed with UKIRT (including five from outside LRL, but which we have argued are not significantly different) should therefore be accompanied by a ‘virtual’ sample of 12.5 quasars.

### 3 IMAGING OBSERVATIONS

All objects were observed at UKIRT using the IRCAM3 infrared array with a nominal scale of  $0''.281 \text{ pixel}^{-1}$ . Our observing strategy consisted of dithering the telescope to place the object in nine different locations on the detector array, and after applying a linearity correction to each frame, we reduced the data in the following manner. First, each of the nine frames was dark-subtracted, and all the frames were then scaled to have the same median pixel value and median-filtered to produce a flat field. This was normalized and then divided into the individual dark-subtracted frames. These frames were registered at  $J$  and  $K$  by determining the individual image offsets from the centroids of the brightest objects in the fields where possible, and otherwise (e.g. at  $L'$ , where the high thermal background and smaller field of view made it impossible to see anything in the individual images) by using the telescope offsets recorded in the image headers. Each set of nine images was then averaged together (ignoring known bad pixels), and objects identified in this image as contiguous groups of pixels whose values were above a certain threshold determined from the sky level and noise. A new flat field was then constructed, ignoring the regions in the individual frames which contained objects, and the above procedure was repeated. Usually we took more than one set of nine images, and the final image was produced by averaging these sets, after additional registration if necessary. Flux calibration was usually performed by observing several UKIRT flux standards during the course of each night and determining the atmospheric extinction coefficient and array sensitivity in each filter. The  $L'$  image of

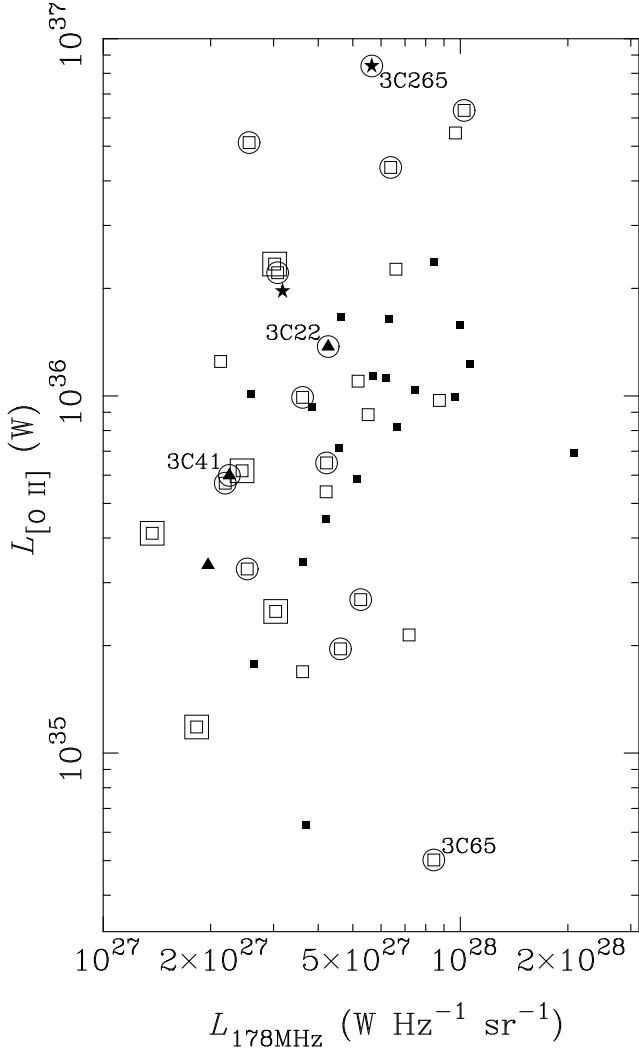


**Figure 4.** [O II]  $\lambda 3727$  narrow-line luminosity versus 178 MHz radio luminosity for objects from the LRL sample with  $0.65 \leq z < 1.20$  plus the additional UKIRT targets. Symbols have the same meaning as in Fig. 3. Emission line data are taken from the compilation of Jackson & Rawlings (1997) with a few updates reported by Willott et al. (1998c); six objects without [O II] measurements have had their [O III] luminosities scaled according to the typical line ratios in McCarthy (1993); an [O II] rest-frame equivalent width of  $10 \text{ \AA}$  has been assumed for the seven quasars without spectrophotometry, and four objects (3C 220.3, 3C 292, 3C 318 and 3C 325) have not been plotted due to the lack of any emission line data.

3C 22 was calibrated using observations of the single standard star HD 225023 taken immediately before and after the radio galaxy images.

Our initial observing run of UT 1995 March 23–26 was beset by problems with the IRCAM3 control software, ALICE. Not only did this result in a significant loss of observing time, but our  $L'$  images frequently showed residual gradients and other structure due to an unstable bias level. We excluded from the final coaddition those images which were most seriously affected by this problem, but in many cases the images could be reduced in the normal manner and the only effect was an increased noise level which caused the

**Table 2.** Observing log. Listed for each filter and each source are the UT date of observation (YYMMDD) and total useful exposure time (in seconds).  $K$ -band imaging of 3C54 was accidentally excluded from the observing programme.

Name	$z$	$J$		$K$		$L'$	
3C 22	0.935	970826	540	970826	540	970130	540
3C 34	0.690	970825	1080	970825	1080	970825	3510
3C 41	0.794	961104	1080	961104	900	961104	3240
3C 44	0.660	970824	1080	970824	1080	970825	3240
3C 54	0.827	970826	2160			970826	3510
3C 55	0.735	970824	1080	970824	1080	970824	3510
3C 65	1.176	961104	1080	961104	1080	961104	3240
3C 107	0.785	970824	1080	970824	1080	970826	3510
3C 114	0.815	970824	1080	970824	1080	970825	3240
3C 217	0.898	950324	810	950324	810	950324	1820
3C 226	0.818	950323	810	950323	810	950323	1960
3C 265	0.811	950323	810	950323	810	950324	2630
3C 272	0.944	950323	810	950323	810	950324	2540
3C 289	0.967	950325	810	950325	810	950325	2120
3C 340	0.775	970825	1080	970825	1080	970825	3510
3C 352	0.807	950325	810	950325	810	950325	1980
3C 356	1.079	970825	4860	950323	4860	970824	3660
3C 368	1.132	970914	1080	970914	1080	970914	3510
3C 441	0.707	970824	1080	970824	1080	970824	3390

overall signal-to-noise ratio to increase more slowly than the square root of the total integration time. For this reason, our sensitivity at  $L'$  during this run was lower than during later runs (where this problem was not experienced), even though a number of sources received similar total exposure times. We present our complete observing log in Table 2.

Of those objects observed during the 1995 run, only 3C 265 was detected, and was extended over several arcseconds east–west. Since this is not a preferred axis of the host galaxy or radio source, we suspected that the elongation may have been caused by telescope drift during the two hours over which our observation was made. This was confirmed by our 3C 356 images, which were taken over approximately two hours of real time, and therefore allowed us to measure the true image offsets from sources on the frames and compare them to the nominal telescope values. A drift of  $\sim 0.9 \text{ arcsec hr}^{-1}$  in an easterly direction was revealed, and the 3C 265 data were re-reduced with this drift accounted for. The new image revealed a bright source, this time only slightly elongated in an east–west direction. We attribute this elongation to imperfect correction of the telescope drift and believe the source to be unresolved. We re-reduced the other  $L'$  datasets incorporating the telescope drift correction, but failed to detect any of the remaining objects. The addition of the fast guider and tip-tilt secondary mirror for the later observations meant that those images were not affected in this manner.

## 4 RESULTS AND ANALYSIS

In Table 3 we present the results of photometry in 3-arcsec and 6-arcsec apertures for the galaxies observed. Although some of the limits at  $L'$  are fairly bright ( $L' < 15.5$ ) due to the reduced exposure times caused by the problems with the instrument electronics, most observations were not af-

**Table 3.** Aperture photometry (converted to zero airmass) from our UKIRT images. All limits are  $2.5\sigma$ . Sources marked \* are not members of LRL, only 3CR.

Name	$z$	$J$ ( $3''$ )	$K$ ( $3''$ )	$L'$ ( $3''$ )	$J$ ( $6''$ )	$K$ ( $6''$ )	$L'$ ( $6''$ )
3C 22	0.935	$17.71 \pm 0.02$	$15.74 \pm 0.03$	$13.34 \pm 0.14$	$17.47 \pm 0.03$	$15.57 \pm 0.03$	$13.23 \pm 0.21$
3C 34	0.690	$18.53 \pm 0.02$	$16.66 \pm 0.02$	$> 15.72$	$18.05 \pm 0.03$	$16.20 \pm 0.03$	$> 14.97$
3C 41	0.794	$18.38 \pm 0.06$	$16.17 \pm 0.05$	$13.71 \pm 0.13$	$17.93 \pm 0.06$	$15.87 \pm 0.05$	$13.49 \pm 0.20$
3C 44*	0.660	$18.24 \pm 0.03$	$16.51 \pm 0.03$	$> 15.75$	$17.75 \pm 0.03$	$16.09 \pm 0.03$	$> 15.00$
3C 54*	0.827	$18.69 \pm 0.03$		$> 15.60$	$18.20 \pm 0.03$		$> 14.85$
3C 55	0.735	$18.92 \pm 0.04$	$17.69 \pm 0.04$	$> 15.84$	$18.57 \pm 0.05$	$17.40 \pm 0.06$	$> 15.09$
3C 65	1.176	$19.36 \pm 0.07$	$17.25 \pm 0.05$	$15.53 \pm 0.49$	$18.90 \pm 0.08$	$16.83 \pm 0.06$	$> 14.80$
3C 107*	0.785	$19.24 \pm 0.05$	$17.36 \pm 0.04$	$> 15.57$	$18.95 \pm 0.07$	$17.13 \pm 0.05$	$> 14.82$
3C 114*	0.815	$19.24 \pm 0.05$	$16.95 \pm 0.03$	$> 15.72$	$18.75 \pm 0.06$	$16.46 \pm 0.03$	$> 14.97$
3C 217	0.898	$19.12 \pm 0.04$	$18.14 \pm 0.07$	$> 15.32$	$18.75 \pm 0.05$	$17.68 \pm 0.09$	$> 14.57$
3C 226	0.818	$18.88 \pm 0.05$	$17.08 \pm 0.04$	$> 15.41$	$18.39 \pm 0.06$	$16.76 \pm 0.05$	$> 14.66$
3C 265	0.811	$18.09 \pm 0.04$	$16.67 \pm 0.03$	$14.04 \pm 0.13$	$17.66 \pm 0.04$	$16.35 \pm 0.04$	$13.94 \pm 0.22$
3C 272*	0.944	$19.06 \pm 0.05$	$17.14 \pm 0.04$	$> 15.39$	$18.88 \pm 0.06$	$16.86 \pm 0.05$	$> 14.64$
3C 289	0.967	$18.94 \pm 0.04$	$17.31 \pm 0.05$	$> 15.47$	$18.34 \pm 0.04$	$16.79 \pm 0.06$	$> 14.72$
3C 340	0.775	$18.94 \pm 0.03$	$17.25 \pm 0.03$	$> 15.70$	$18.64 \pm 0.05$	$17.12 \pm 0.05$	$> 14.95$
3C 352	0.807	$18.69 \pm 0.03$	$17.32 \pm 0.05$	$> 15.41$	$18.06 \pm 0.03$	$16.84 \pm 0.06$	$> 14.66$
3C 356a	1.079	$19.34 \pm 0.03$	$17.57 \pm 0.03$	$> 15.65$	$18.92 \pm 0.03$	$17.18 \pm 0.04$	$> 14.90$
3C 356b	1.079	$19.40 \pm 0.03$	$17.47 \pm 0.03$	$> 15.65$	$18.74 \pm 0.03$	$16.86 \pm 0.03$	$> 14.90$
3C 368 <sup>†</sup>	1.132	$19.91 \pm 0.18$	$18.12 \pm 0.15$	$> 15.79$	$19.26 \pm 0.29$	$17.55 \pm 0.23$	$> 15.04$
3C 441	0.707	$18.48 \pm 0.03$	$16.76 \pm 0.03$	$> 15.80$	$18.00 \pm 0.04$	$16.32 \pm 0.03$	$> 15.05$

<sup>†</sup> We have subtracted the foreground Galactic star and assumed that the nucleus is at the location identified by Stockton, Ridgway & Kellogg (1996).

fects and the limits provide useful constraints as detailed in Section 6.

Aperture photometry of our images at  $J$  and  $K$  agrees well with that of Best et al. (1998), with an r.m.s. difference of 0.10 mag and no tendency for our magnitudes to be systematically fainter or brighter. The agreement with the aperture photometry of Lilly & Longair (1984) is also good, although the uncertainties in their measurements are often large. We note that errors at the level of 0.1 mag are insufficient to affect our results. Four radio galaxies were detected at  $L'$ , and we present our  $JKL'$  images of these, together with an optical *HST* image of each, in Fig. 5.

In Fig. 6 we present our photometry graphically in a colour–colour diagram. We also plot the loci for combinations of reddened quasar plus unreddened starlight. This figure can be used to make an approximate determination of the nature of individual sources; for example, 3C 22 and 3C 41 are clearly lightly reddened ( $A_V \approx 2$ –5) quasars, whereas 3C 34 and 3C 44 appear to be normal galaxies with no sign of AGN activity in their infrared photometry. However, some objects, such as 3C 55, are more ambiguous, but this ambiguity can be removed by considering both the  $K$ -band morphology and the  $L'$ -band magnitude of such sources. Considering 3C 55, it is more than two magnitudes fainter at  $K$  than the locus of 3C quasars (Fig. 1), and it is clearly resolved in our near-infrared images, indicating that its putative central quasar does not contribute significantly at these wavelengths. The same line of reasoning can be applied to the other radio galaxies whose  $K - L'$  upper limits do not apparently exclude them from being lightly-reddened quasars in Fig. 6. The case of 3C 65 is rather more ambiguous — for the present, we shall assume that it too is lightly-reddened (see also Lacy et al. 1995).

Although Fig. 6 can be used to estimate directly the extinctions to the quasars in those radio galaxies detected at

**Table 4.** Estimated extinctions and unobscured quasar magnitudes, and estimated fraction of non-stellar emission in a 3-arcsec aperture at  $K$ , determined using the method outlined in Section 4.

Object	$A_V$	$K_0$	$f_K$
3C 22	$3 \pm 1$	$14.77 \pm 0.18$	$0.90^{+0.10}_{-0.12}$
3C 41	$6 \pm 2$	$15.06 \pm 0.21$	$0.51^{+0.13}_{-0.11}$
3C 65	$3 \pm 1$	$17.70 \pm 0.22$	$0.28^{+0.12}_{-0.09}$
3C 265	$15 \pm 4$	$14.31 \pm 0.45$	$0.14^{+0.05}_{-0.06}$

$L'$ , we opt for a less subjective approach. In this method, we adopt various galaxy SEDs (1-Gyr bursts with ages ranging from 1 Gyr to the age of the Universe at the source redshift) and solve for the quasar and galaxy magnitudes and the nuclear extinction, using our  $JKL'$  photometry. As Fig. 2 shows, the  $J - K$  and  $K - L'$  colours are not especially sensitive to age at  $z \sim 1$ , so there is little variation in the derived quantities with the assumed galaxy age. With the added constraint that the  $K$  magnitude of the host galaxy should lie on the  $K$ – $z$  relation, we then determine the range of each parameter. In Table 4 we present the derived nuclear extinctions and unobscured quasar  $K$  magnitudes. We also provide the estimated fraction of  $K$ -band non-stellar light in a 3-arcsec aperture.

## 5 COMPARISON WITH OTHER DATA

### 5.1 Re-analysis of *HST* data

Although we have obtained extinction estimates from our infrared data alone, they are rather uncertain and we would also like to be able to confirm the correctness of our values. The easiest way to do this is by extending our study to optical wavelengths, and searching for point sources there.

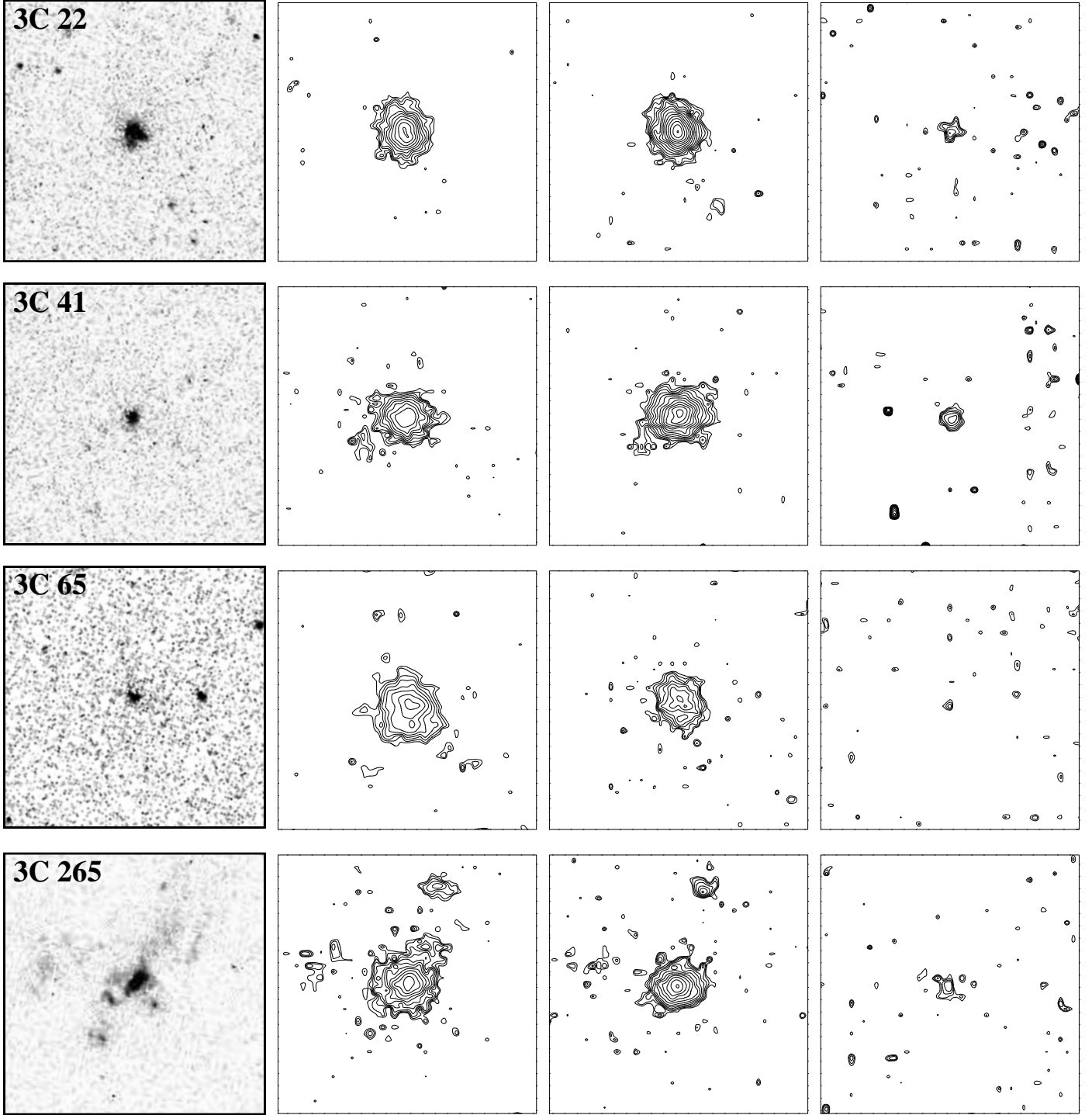


**Figure 5.** Images of the four radio galaxies detected at  $L'$ . The greyscale is an optical *HST* image, and the contour maps are, from left to right,  $J$ ,  $K$ , and  $L'$ , with contours spaced at intervals of  $0.25 \text{ mag arcsec}^{-2}$ . Each field is  $12 \text{ arcsec}$  on a side. The galaxies and the filters in which the *HST* images were taken are, from top to bottom, 3C 22 (F622W), 3C 41 (F555W), 3C 65 (F675W), and 3C 265 (F555W).

However, with the exception of 3C 22, which McCarthy (1988) reported to be unresolved in an optical continuum image, the quasar nuclei in the other objects are predicted to be too faint in the optical ( $V \gtrsim 24$ ) to be readily detectable from ground-based images. We therefore turn to the archived *Hubble Space Telescope* WFPC2 observations

of these objects (PID 1070, P.I. Longair; see Best, Longair & Röttgering 1997) where the point-source sensitivity is much greater. The calibrated science data files were retrieved from the *HST* data archive and each pair of images combined and cleaned of cosmic rays using the IRAF task *crrej*, with pixels unaffected by cosmic rays in both images being assigned an



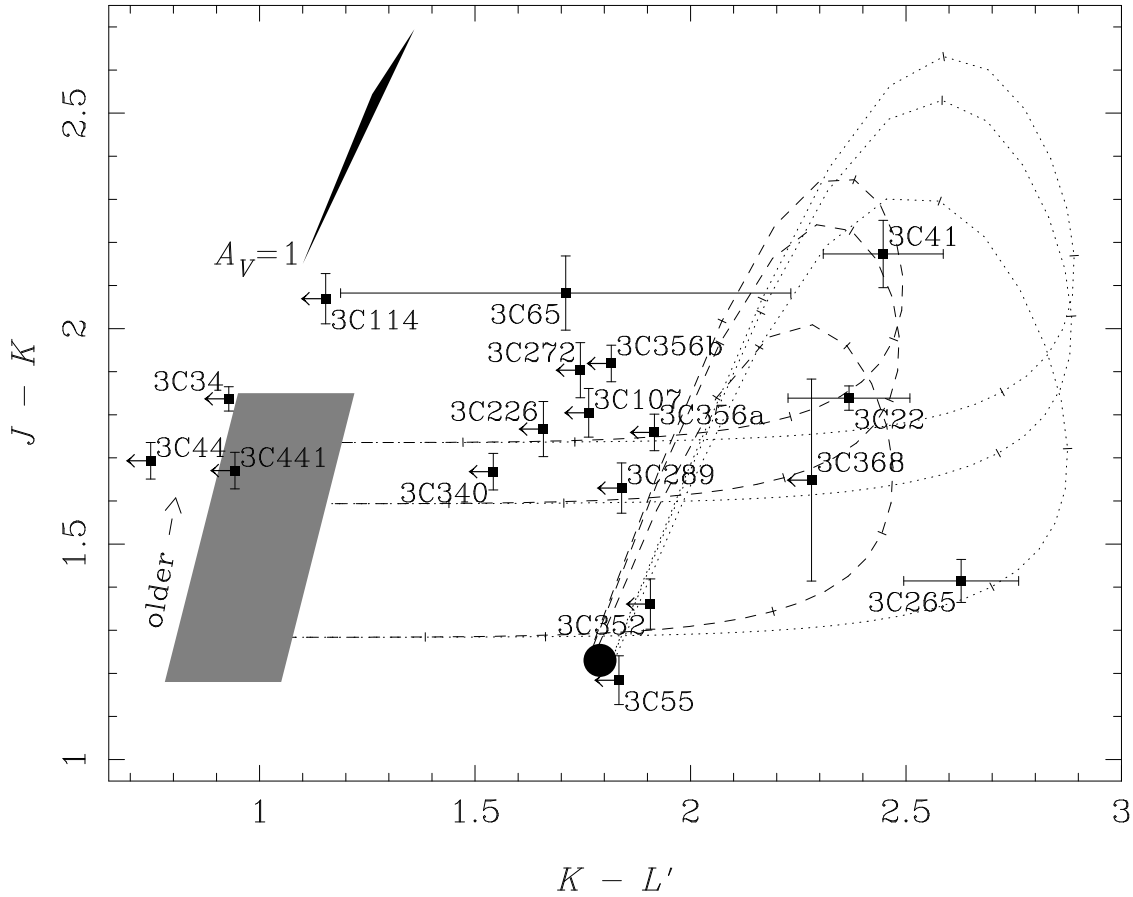


**Figure 6.** Colour-colour diagram for the galaxies observed, as measured in 3-arcsec apertures, and corrected for Galactic extinction using the prescription of Rowan-Robinson et al. (1991). The shaded region on the left indicates the colours of stellar populations formed in a 1-Gyr burst with ages 1–5 Gyr, with older populations being redder in  $J - K$  (as indicated). The solid circle represents the combined colours of an unreddened quasar and stellar population. The dashed lines indicate the loci of colours for a reddened quasar and an unreddened stellar population of ages 1, 2, 5 Gyr at  $z = 1$  (there is little variation in the loci with redshift within the range we are considering) where the quasar is intrinsically five times brighter than the host galaxy in the  $K$ -band. The dotted lines are the loci for the case where the quasar is ten times brighter than its host galaxy. Each curve has tick marks at  $A_V = 2, 5, 10, 15, 30$  mag. The wedge in the top left of the diagram shows the effect of one magnitude of visual extinction at  $0.65 \leq z < 1.20$ .

exposure-time-weighted average. Flux calibration was performed using the on-line WFPC2 exposure time calculator, assuming an  $\alpha = 0$  source spectrum.

We re-analysed these data using our own two-dimensional fitting procedure. Heavy smoothing of the data revealed that a circularly-symmetric de Vaucouleurs (1948) profile provided an adequate fit to the host galaxy component for 3C 22, 3C 41 and 3C 65 while no reasonable galaxy model could fit the very peculiar structure of 3C 265 (see Fig. 5) so no fit was attempted. For the other objects, we fit a model WFPC2 point spread function (generated with the TINY TIM software; Krist 1995) and a de Vaucouleurs host galaxy. The point source flux and the total flux and effective radius of the galaxy component were varied to minimize the value of  $\chi^2$ . The uncertainty assigned to each pixel was calculated as the Poisson error on the source counts added in quadrature to the standard deviation of pixel values measured in a blank region of the chip. Values of  $\chi^2$  (and residual images) were produced as a function of fitting radius to check for systematic effects (such as incorrect background subtraction), and as none were found a fitting radius of 15 pixels

(1.5 arcsec) was used in all cases, and fluxes measured over the same aperture. The residual images were structureless with the exception of 3C 22 for which the two companion objects discussed by Best et al. (1997) were clearly revealed (and possibly the F555W image of 3C 41 where there was some evidence for excess partially-resolved emission near the nucleus); in the case of 3C 22 the fitting procedure was repeated after masking out data at the positions of the companions. The quantitative results of this analysis are presented in Table 5; also listed are the fluxes estimated using the intrinsic nuclear fluxes and extinctions listed in Table 4, accounting for the Galactic extinctions given in Table 6. The exclusion of 3C 265 from this analysis is not a great problem because its predicted transmitted nuclear flux is several orders of magnitude fainter than the detection limit in the *HST* images, and spectropolarimetry (Dey & Spinrad 1996) suggests that any compact component is more likely to be light scattered close to the nucleus. The agreement between predicted and observed *HST* fluxes is generally very good, with the exception of the F555W flux of 3C 41, which is

**Table 5.** The results of our host galaxy plus nuclear point source decomposition performed on the archived *HST* images of the four objects detected at  $L'$ , as described in Section 5.1. Data obtained on 3C 22 using the F1042M filter have extremely poor sensitivity and are ignored. For the best-fitting model in each object/filter combination, we list the reduced  $\chi^2$ , the effective radius  $r_e$  of the host galaxy, the percentage contribution to the *HST* counts within a 3-arcsec diameter from the galaxy and quasar, and the flux density of the quasar component. Note that these percentages typically sum to less than 100 per cent because other components are revealed by the modelling process, and evident in the residual map. Significant differences between our best-fit parameters and those derived from the same *HST* dataset by Best et al. (1998) are discussed in Section 5.1. Also listed is the flux density of the quasar nucleus estimated from our near-infrared data (see Section 4).

Name	WFPC2 Filter	$\chi^2_\nu$	$r_e$ (arcsec)	% gal	% QSO	Fluxes ( $\mu\text{Jy}$ )	
						Observed	Estimated
3C 22	F622W	3.3	0.8	80	15	1.8	$3.01^{+8.04}_{-2.19}$
3C 41	F555W	2.0	0.6	60	30	1.3	$0.03^{+0.13}_{-0.02}$
	F785LP	2.5	0.8	90	10	2.8	$0.89^{+2.12}_{-0.52}$
3C 65	F675W	1.3	1.2	> 90	< 10	< 0.2	$0.33^{+0.76}_{-0.23}$
	F814W	1.0	1.5	> 90	< 10	< 0.7	$0.74^{+1.27}_{-0.47}$

predicted to be much fainter than is observed. We discuss this difference below.

It is worth noting some differences in our fitting results to those obtained previously by Best et al. (1998) using a one-dimensional fitting algorithm on the same dataset. While we obtain similar results for 3C 65, our effective radii for 3C 22 and 3C 41 are much smaller than those of Best et al. We suggest that these authors have overestimated the radii in these galaxies because their bright nuclei force them to exclude all data within a radius of 1 arcsec, and the fit is therefore dominated by the very tenuous detection of the low-surface brightness extended starlight — their outermost datapoints correspond to fluxes per pixel well below one-tenth of the sky noise. At these levels, one cannot remove all the companion objects, and there will also be low-energy cosmic rays left in the final image, with the result that the surface brightness will be overestimated, leading in turn to an overestimate of the effective radius. Fitting the host and nucleus simultaneously using the full two-dimensional data alleviates all of these concerns, allowing data from the central regions to constrain  $r_e$  as well as giving a very low weight to individual discrepant pixels at large radii.

After using the *HST* data to isolate compact components in the optical it was possible to make more detailed studies of the SEDs, and hence better estimates of the nuclear extinctions of our UKIRT  $L'$  detections. A minimum- $\chi^2$  fitting procedure was used to find the most likely values of  $A_V$ , and the fractions of nuclear flux in 3-arcsec apertures at  $J$ ,  $H$  and  $K$ . In performing this analysis, we assumed that the  $L'$  and *HST* point source fluxes are dominated by transmitted light from the reddened quasar nucleus, except for 3C 41 where we make a correction for scattered light described below. The results of this analysis are presented in Fig. 7 and Table 6. We estimated errors on the fitted quantities by varying the intrinsic colour of the quasar over the range observed in naked quasars accounting properly for the photometric error on each (assumed) nuclear flux data point (see Fig. 7); there were no significant differences in the derived quantities from fits which used LMC- and SMC-type dust extinction curves (from Pei 1992). Note the extremely good agreement between the extinction estimates, and especially the fractions of non-stellar  $K$ -band light, determined from the infrared data alone (Table 4) and the more refined values incorporating the *HST* data (Table 6). This indicates

the ability of infrared imaging alone to provide quantitative, as well as qualitative, statements about the nature of radio galaxies. Throughout the remainder of this paper, we adopt the extinction estimates listed in Table 6 in preference to those of Table 4. Brief notes on an object-by-object basis follow.

## 5.2 Notes on individual objects

**3C 22** A seemingly straightforward case of a nucleus reddened by  $A_V = 3.6 \pm 0.3$  which contributes  $\sim 80$  per cent of the 3-arcsec aperture  $K$ -band light, and dominates the unresolved component in the *HST* data. The lack of optical polarization (see Leyshon & Eales 1998) supports this picture. The extended near-infrared light is presumably from the host galaxy which is clearly visible in the *HST* image.

**3C 41** As we mentioned in Section 5.1, the observed optical fluxes of the compact nucleus are much larger than we inferred from our infrared imaging, suggesting the presence of an additional component, such as scattered light from the nucleus. This is supported by the observed polarization properties of 3C 41 reported in Leyshon & Eales (1998), where the  $V$ -band polarization is  $P = 9.3 \pm 2.3\%$ . For electron-scattering over a small range of angles about a mean angle,  $\theta$ , the intrinsic polarization of electron-scattered radiation is  $P = 100\% \times (1 - \cos^2 \theta) / (1 + \cos^2 \theta)$ , and as a lightly-reddened quasar, the viewing angle should be only slightly larger than the critical angle of the torus,  $\theta_c = 53^\circ$ . Therefore the intrinsic polarization of the scattered light should be around 50%, and approximately one-fifth of the total F555W flux (i.e.,  $\sim 1 \mu\text{Jy}$ ) would need to be scattered to produce the observed fractional polarization. This fraction may be larger if the observed polarization has been diluted by virtue of being averaged over a range of scattering angles, or if the scattering medium is dust. If the scatterers have an asymmetric distribution within the illumination cones, our estimate of the scattering angle will be in error, although this could serve to either increase or decrease the intrinsic polarization. In order to perform a quantitative analysis, however, we assume that this is the true contribution of scattered light. The contribution from scattered light in the F785LP filter is predicted to be similar (from Fig. 4 of Leyshon & Eales 1998), and we therefore fit the SED after subtracting  $1 \mu\text{Jy}$  from each of the two *HST* point source fluxes to ac-

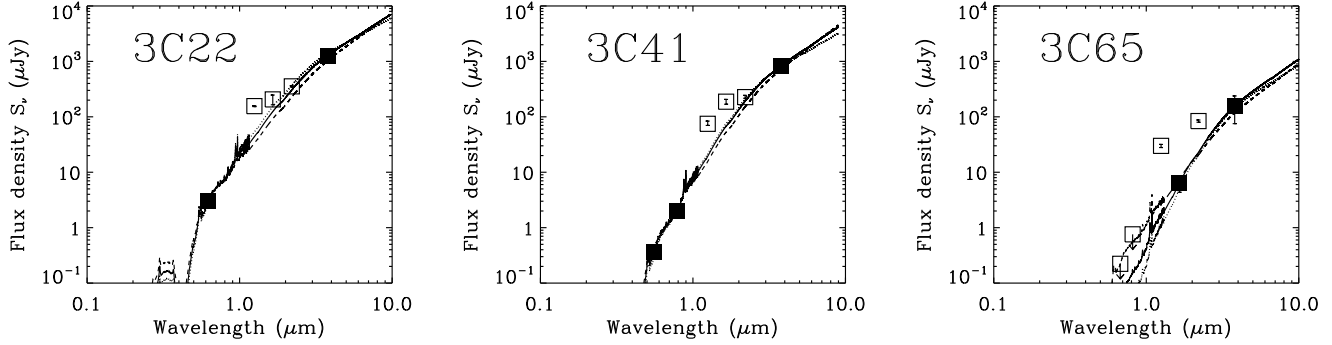


**Figure 7.** Spectral energy distributions (SEDs) for 3C 22, 3C 41, and 3C 65. The data have been corrected for extinction in the Milky Way using the extinction values given in Table 6, and are taken from this paper, Lilly & Longair (1984) and, in the case of 3C 65, Rigler & Lilly (1994). Filled data symbols represent points where we have assumed that all the flux is transmitted light from the quasar nucleus. The full line represents a fit using the canonical quasar spectra reddened using a MW-type extinction curve (full lines). The dotted line is the most-reddened quasar fit consistent with the data allowing the intrinsic SED for the quasar to be bluer by subtracting 0.3 from the spectral index of both the power-law components discussed in Section 1, and the dashed line the least-reddened quasar fit consistent with the data with a redder intrinsic SED (produced by adding 0.3 to both spectral indices). These assumptions about the spread in the intrinsic SEDs are based on the quasar SED study of Neugebauer et al. (1987).

**Table 6.** Results of our fits to the observed spectral energy distributions of 3C 22, 3C 41, and 3C 65: the nuclear extinction and fractional contributions of the quasar nucleus in the *JHK* infrared bands in 3-arcsec apertures are listed. The Galactic extinction,  $A_V$  (MW), has been estimated from the *IRAS* 100  $\mu\text{m}$  maps obtained through *SkyView* (McGlynn, Scolick & White 1996) and the prescription of Rowan-Robinson et al. (1991). Note a typographical error in the value of the Galactic extinction for 3C 22 listed in the caption to Figure 3 of Rawlings et al. (1995).

Name	$A_V$ (MW)	$A_V$	$f_J$	$f_H$	$f_K$
3C 22	0.66	$3.6 \pm 0.3$	$0.30 \pm 0.10$	$0.70 \pm 0.20$	$0.85 \pm 0.15$
3C 41	0.20	$4.4 \pm 0.4$	$0.25 \pm 0.05$	$0.35 \pm 0.10$	$0.75 \pm 0.20$
3C 65	0.15	$4.8 \pm 1.3$	$0.06 \pm 0.05$	$0.10^\ddagger$	$0.25 \pm 0.05$

$^\ddagger$ Following Rigler & Lilly (1994) we have assumed that 10% of the *H*-band flux measured by Lilly & Longair (1984) lies in a nuclear component arising from reddened transmitted quasar light.

count for the scattered component. We find  $A_V = 4.4 \pm 0.4$  and a transmitted quasar light contribution of  $\sim 85\%$  to the 3-arcsec aperture *K*-band emission. As was the case for 3C 22, the extended near-infrared light can be ascribed to the host galaxy mapped in the *HST* image.

**3C 65** There are two reasons why it remains uncertain whether we have detected non-stellar emission at  $L'$  in this object. First, the detection itself is significant only at the  $2.7\sigma$  level and then only in the 3-arcsec aperture. Secondly, the separation between the location of 3C 65 and possible loci of stellar populations in Fig. 6 is only marginally significant. However, both Lacy et al. (1995) and Stockton, Kellogg & Ridgway (1995) have argued previously for the presence of a quasar nucleus, and most importantly for our purposes an analysis by Rigler & Lilly (1994) of a 0.6-arcsec resolution *H*-band image points to a nuclear component contributing  $\sim 10\%$  of the flux. Our SED fit uses this point, the  $L'$  detection and the *HST* limits to suggest that there is indeed a quasar present which has  $A_V = 4.8 \pm 1.3$ . As suggested previously by Lacy et al. (1995), 3C 65 seems to have an unusually faint quasar nucleus for a powerful radio source. In the absence of reddening we estimate that it would have  $M_B = -24.8$ , 1.5 mag fainter than the intrinsic luminosity of the 3C 22 quasar and 0.6 mag fainter than the 3C 41 quasar. Note that 3C 65 is a prominent outlier in Fig. 4 in the sense that its narrow emission line luminosity lies factors

of 26 and 11 below the line luminosities of 3C 22 and 3C 41, respectively.

**3C 265** Although the complex optical structure of 3C 265 excludes an analysis of the *HST* data, a visual inspection of the images indicates that no point source is present at the location of the nucleus, supporting our higher extinction estimate of  $A_V \approx 15$  for this source. The fact that 3C 265 is convincingly detected at  $L'$  despite such large extinction is undoubtedly due to the very luminous quasar it contains, as evidenced by its line luminosity (Fig. 4). Although this source displays strong, extended optical polarization (Jannuzi & Elston 1991), the near-infrared polarization is lower ( $\sim 5\%$  in the *H*-band; Jannuzi, private communication). The thermal-infrared polarization is likely to be even lower, since the overall SED of 3C 265 rises more rapidly in the thermal-IR than a quasar SED. Even assuming electron scattering, the scattered nuclear component cannot contribute more than  $\sim (3/f)\%$  of the  $L'$ -band flux, where  $f$  is the fractional polarization of the scattered component, unless it too is heavily reddened. We are therefore confident that our  $L'$  detection of this source represents the true, transmitted quasar continuum.

**Table 7.** Results of four-Gaussian fit to the continuum-subtracted spectrum of 3C 41. The line widths have not been corrected for the instrumental resolution of  $300 \text{ km s}^{-1}$ .

Line	Redshift	Flux ( $10^{-19} \text{ W m}^{-2}$ )	FWHM ( $\text{km s}^{-1}$ )
$\text{H}\alpha_n$	$0.7929 \pm 0.0005$	$5.06 \pm 0.81$	$771 \pm 111$
$[\text{N II}]^a$	$0.7911 \pm 0.0008$	$2.83 \pm 0.74$	$695 \pm 178$
$\text{H}\alpha_b$	$0.7964 \pm 0.0010$	$21.25 \pm 1.67$	$3438 \pm 335$

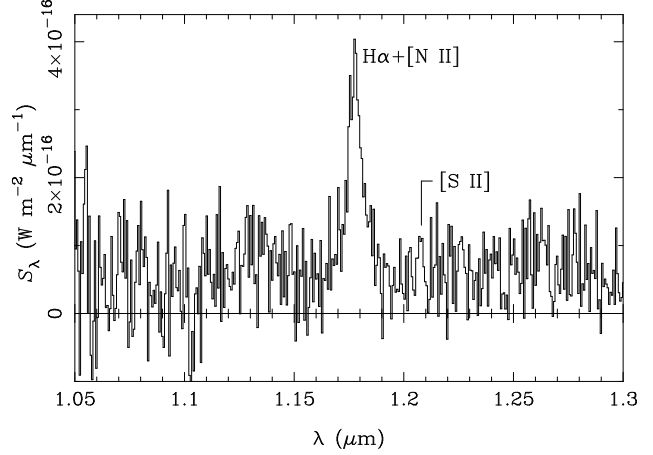
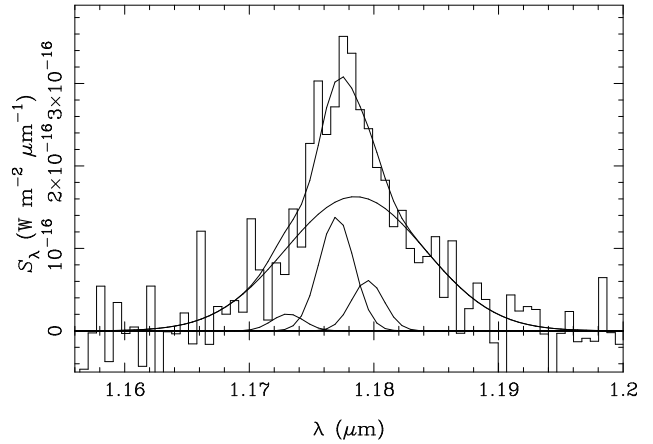
<sup>a</sup>  $\lambda 6584$  only.

### 5.3 $\text{H}\alpha$ spectroscopy

As we mentioned in Section 1, a low value of the nuclear reddening may be indicated by broad wings on the  $\text{H}\alpha$  emission line, which is redshifted into the  $J$  window for 3C 22, 3C 41 and 3C 265 (but lies where the atmosphere is opaque for 3C 65). Economou et al. (1995) and Rawlings et al. (1995) have both shown the existence of broad  $\text{H}\alpha$  in 3C 22, and inferred low values of the extinction ( $A_V < 4$  and  $A_V = 2 \pm 1$ , respectively), in agreement with our own estimate. Given the relatively low line of sight extinction derived for the quasar within 3C 41, we took a  $J$ -band spectrum with CGS4 on UKIRT on the night of UT 1997 August 12 to look for broad  $\text{H}\alpha$ . We used the standard ‘ABBA’ technique (e.g., Eales & Rawlings 1993) for observing the source, keeping it on the array at all times so that all 48 minutes of integration contributed to the object signal. The 75 lines  $\text{mm}^{-1}$  grating was used in second order with the short camera and a 1-pixel (1.22-arcsec) slit to provide a resolving power of  $\lambda/\Delta\lambda \approx 1000$  at the wavelength of  $\text{H}\alpha$ . We used  $2 \times 2$  over-sampling and the spectra were interleaved with bad pixel masking using the CGS4DR software package before being exported to IRAF for coaddition, sky-subtraction, and extraction of the one-dimensional spectra. The final reduced spectrum (extracted from a 1.22-arcsec square aperture) is presented in Fig. 8. Broad wings are clearly visible on the  $\text{H}\alpha$  line. The convolution of this spectrum with the UKIRT  $J$  filter gives a synthetic magnitude  $J = 19.13$ , which agrees well with the value  $J = 19.29$  determined from our image, given that the image was taken in poorer seeing.

We have analysed the spectrum of 3C 41 to derive an independent extinction estimate. First a fit was made to the continuum using ten cubic spline pieces and subtracted from the data. We then used the SPECFIT package (Kriss 1994) to fit the  $\text{H}\alpha + [\text{N II}]$  blend with a combination of four Gaussians, representing the three narrow lines and a broad  $\text{H}\alpha$  component. We fixed the relative wavelengths and intensities of the  $[\text{N II}]$  lines and demanded that they have the same width, but allowed the other parameters to vary freely. The results are presented in Fig. 9 and Table 7.

The results of our line fitting are very similar to those found by Economou et al. (1995) for 3C 22, namely: a rest-frame equivalent width of  $470 \text{ \AA}$  for the blend (*cf.*  $540 \text{ \AA}$  for 3C 22); a relative redshift of  $1050 \text{ km s}^{-1}$  ( $960 \text{ km s}^{-1}$ ) for the broad  $\text{H}\alpha$  line with respect to the narrow line; and ratios  $[\text{N II}] \lambda 6584/\text{H}\alpha = 0.56 \pm 0.17$  ( $0.59 \pm 0.14$ ) and  $\text{H}\alpha_b/\text{H}\alpha_n = 4.19 \pm 0.75$  ( $3.92 \pm 0.49$ ). Assuming an intrinsic ratio of broad to narrow  $\text{H}\alpha$  of 40 (e.g., Jackson & Eracleous 1995), this implies  $A_V \approx 3$  as the differential extinction between the broad and narrow lines, in fair agreement with our more refined estimate from the spectral energy distribution.

**Figure 8.**  $J$ -band spectrum of 3C 41. Note the broad base to the  $\text{H}\alpha + [\text{N II}]$  complex and the apparent detection of  $[\text{S II}]$ .**Figure 9.** Continuum-subtracted  $J$ -band spectrum of 3C 41 and best fit of Gaussian lines, as described in the text.

While Economou et al. (1998) have also used CGS4 to detect broad wings on the  $\text{H}\alpha$  line in 3C 41, their spectrum of 3C 265 does not reveal a broad line. This non-detection is in agreement with the much larger extinction we derive to the quasar in this object.

## 6 DISCUSSION

In Fig. 10 we plot the  $L'$  magnitudes and limits of our UKIRT targets against redshift, and compare these data with reddened quasar spectra. We also plot the estimated  $L'$  magnitudes of the LRL quasars in the same redshift range, extrapolated from optical (usually  $V$ -band) magnitudes, assuming zero reddening. Because the differential reddening between (observed-frame)  $V$  and  $L'$  is large (approximately 2 mag for  $A_V = 1$ ), even modest amounts of extinction will move the quasars up the diagram significantly. Indeed, the two apparently faint quasars at high redshift are 3C 212 and 3C 190, which are both intrinsically red (Smith & Spinrad 1980) and will therefore be much brighter at  $L'$  than we have estimated.

Bearing this in mind, it is clear that our  $L'$  limits are

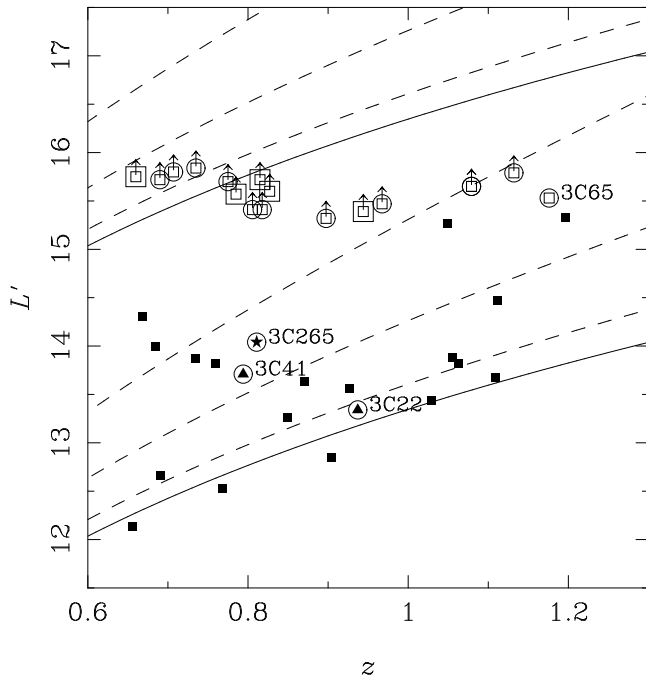


**Figure 10.** The  $L'$  versus redshift plane for the LRL quasars plus our sample of radio galaxies; symbols have the same meaning as in Fig. 3.  $L'$  magnitudes for the LRL quasars have been estimated from the optical magnitudes listed in LRL (except for 3C 190 where LRL list a photographic magnitude, and we elect to use the *HST* magnitude of de Vries et al. 1997), using the canonical quasar spectrum to extrapolate to longer wavelengths. We exclude 3C 343 from this plot since, although classified as a quasar by LRL, it is clearly resolved by de Vries et al. (1997). The solid lines show the loci of quasars with the canonical spectrum and no reddening for two values of absolute magnitude ( $M_B = -26$  for the lower curve,  $M_B = -23$  for the upper). The dashed lines show the loci of the same quasars reddened internally by  $A_V = 2, 7$  and 15.

much fainter than the loci of unreddened quasars with luminosities typical of powerful radio sources at these redshifts. We have also been able to detect the weakest quasars associated with such objects, like 3C 65, although at poorer limiting values of  $A_V \lesssim 5$ . However, the distribution of narrow emission line luminosities (Fig. 4) suggests that there are very few, if any, other objects as weak as 3C 65 in the LRL sample at these redshifts. Assuming then that the quasars within the many radio galaxies for which we only have limits at  $L'$  have luminosities typical of those within other powerful radio sources, Fig. 10 makes it clear that the extinction must be large in those sources we failed to detect at  $L'$ .

Our data can be used to quantify the size of the dust-reddened quasar population. Since all our sources are steep-spectrum objects, red objects in our sample are unlikely to be due to beamed synchrotron radiation, as has been suggested for the red flat-spectrum quasar population (Serjeant & Rawlings 1996; Benn et al. 1998). Among the 18 sources classified as quasars in Fig. 10, there are two (3C 190 and 3C 212; Smith & Spinrad 1980) that fall into this category. Scaling this to our complete sample of 12.5 ‘virtual’ quasars, and adding in 3C 22, 3C 41, and 3C 65, we find that  $28^{+25}_{-13}\%$  of quasars are dust-reddened (90% confidence limits).

### 6.1 Influence of quasar nuclei on the $K$ - $z$ relation for radio galaxies

Our first goal for this project was to investigate whether the presence of reddened quasar light accounts for a significant fraction of the total  $K$ -band flux in 3C radio galaxies. This could provide an explanation for the brighter  $K$  magnitudes displayed by 3C radio galaxies compared to those from the fainter 6C and B2 samples (Eales et al. 1997). We have therefore undertaken a similar analysis to that of Eales et al., which involves fitting the least-squares regression line to the 3C  $K$ -band data, and then examining the residuals about this line for both the 3C and 6C samples (we do not supplement the fainter sample with galaxies from the B2 survey). We use the same 63.9 kpc metric aperture as Eales et al. and use the same prescription for correcting measurements made in apertures of other sizes.

We first confirm the representative nature of our sample by fitting a regression line to the  $K$ -band magnitudes of our 18 galaxies. All 13 galaxies from the 6C survey in the same redshift range ( $0.65 \leq z < 1.20$ ) lie above this line (i.e., they are fainter), with the mean difference being 0.72 mag. This is in good agreement with the 0.59 mag discrepancy found by Eales et al. (1997), and we can use a Kolmogorov-Smirnov test to rule out the hypothesis that both samples are drawn from the same distribution at better than 95% confidence.

We then correct the photometry for the presence of reddened nuclear light, using the fractional contamination determined in Section 5.1 and repeat the process. This time the 6C galaxies are on average only 0.56 mag (40 per cent) fainter, although the samples are still different at greater than 90% confidence. Our confidence levels are lower than those of Eales et al. (1997) solely because our samples each contain only half the number of objects as theirs.

Coupled with the conclusion of Leyshon & Eales (1998) that scattered light is not a major contributor to the total  $K$ -band flux of most 3C radio galaxies, our analysis is able to rule out quasar light as the cause of the correlation between radio luminosity and near-infrared magnitude at  $z \sim 1$ . Emission lines can also be ruled out since they would need to have a total flux of  $\sim 2 \times 10^{-17} \text{ W m}^{-2}$  to provide one-third of the total  $K$ -band light — this is several times greater than the flux of the [O III]  $\lambda\lambda 4959, 5007$  doublet yet the strongest lines which fall into the  $K$ -band over our redshift range are intrinsically much fainter (see also Rawlings et al. 1998a). Finally, the nebular emission which has been suggested provides a significant fraction of the optical light and might explain the alignment effect (Dickson et al. 1995) is a negligible contributor at near-infrared wavelengths. Assuming [O II]/H $\beta \approx 4$  (McCarthy 1993), it can contribute no more than about one per cent of the total  $K$ -band flux.

The ‘extra’ component in 3C radio galaxies, compared to 6C radio galaxies, is therefore not directly related to the more luminous central quasar, and must be additional stellar luminosity, and presumably stellar mass, in the host galaxy. This fits together with the smaller linear sizes of 6C radio galaxy hosts measured by Roche et al. (1998). Plausible reasons why a correlation between host galaxy mass and radio luminosity is seen at  $z \sim 1$ , but not at lower redshifts, are given by Best et al. (1998).

Finally, we note that the r.m.s. deviation of the 3C galaxies about the regression line is reduced from 0.59 to

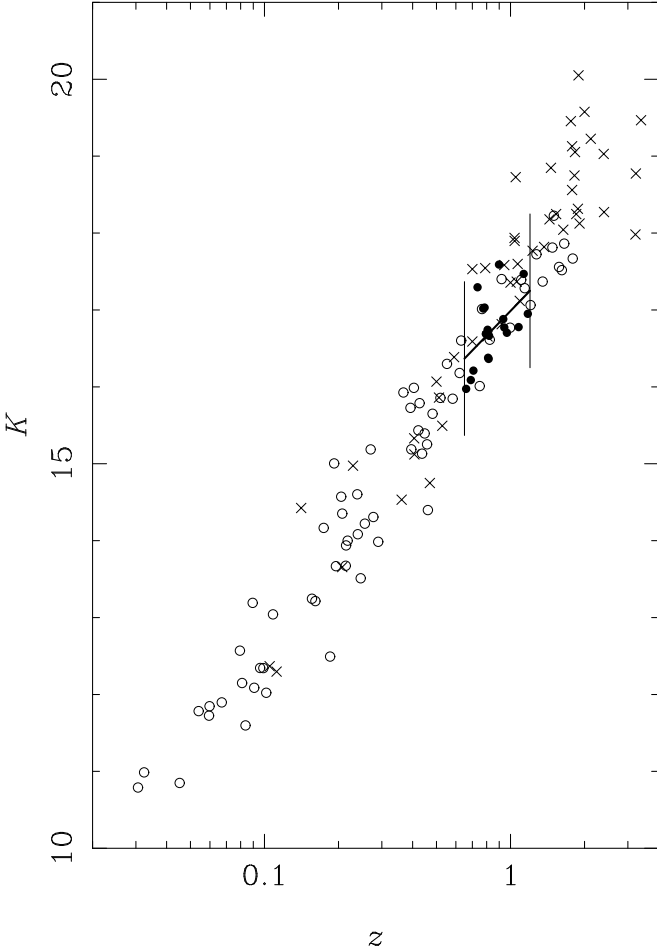


**Figure 11.** Modified  $K$ -band Hubble diagram for radio galaxies from the LRL and 6C samples (open circles and crosses respectively). The solid circles are our sample of 18 galaxies with  $K$ -band photometry, after correction for reddened quasar light. The two vertical lines delineate the redshift range of our sample ( $0.65 \leq z < 1.20$ ) and the heavy line between them is the least-squares fit to the corrected magnitudes. See Figure 1 for references for the photometry.

0.43 magnitudes when the correction for non-stellar contamination is made. This reduced scatter is the same as that observed around Eales et al.'s (1997) least-squares regression line for  $z < 0.6$ .

## 6.2 Test of the receding torus model

In order to be able to compare the receding torus model to our observational data, we have to associate lower limits to the nuclear extinction with the radio galaxies which we failed to detect at  $L'$ . Estimating these extinctions is a very uncertain affair, since we do not know their intrinsic luminosities. Table 4 indicates that a ‘typical’ source might have  $L'_0 \approx 13$  ( $K - L' = 1.87$  for our canonical spectrum at all redshifts  $z < 1.2$ ), yet the quasar within 3C 65 appears to be nearly ten times fainter, and the  $z = 0.768$  quasar 3C 175 is a magnitude brighter (Simpson, unpublished). We adopt  $L'_0 = 13.5$  so that the undetected sources must have  $A_{L'} \gtrsim 2$ , or  $A_V \gtrsim 15$  (at  $z = 1.2$ ; at lower red-

shifts, the rest-frame visual extinction will be higher for the same observed-frame  $A_{L'}$ ) and use this limit for all 15 of our non-detections. Fig. 10 clearly shows the conservative nature of this assumption.

The mean radio luminosity of the radio sources with  $0.65 \leq z < 1.20$  plotted in Fig. 4 is about 70 times greater than that of Hill et al.'s (1996)  $0.1 \leq z < 0.2$  sample. Hill et al. infer an opening angle of  $20^\circ$  for their sample and, applying the relationship  $\tan \theta_c \propto L_{178}^{0.3}$ , we expect  $\theta_c = 52^\circ$ , in very good agreement with the value derived directly from the quasar fraction in LRL. Using the same value for the density of the torus,  $n_H$ , as Hill et al., the receding torus model predicts the distribution of extinctions shown by the dotted line in Fig. 12. Although the model does predict fewer lightly-reddened sources than at low redshift ( $\sim 30\%$  with  $A_V < 6$  mag, as opposed to  $\sim 50\%$ ), it still overpredicts the number. By increasing the density of the torus by about an order of magnitude above that derived for Hill et al.'s sample, we can fit the data of Figure 12 with the dashed line. Since this model is required to reproduce both the numbers of naked and lightly-reddened quasars, there is very little additional information in Fig. 12 with which to compare its predictions. We cannot therefore claim any quantitative agreement between the model and our observations.

There are several points to be made about the receding torus model. First, one must be careful when considering objects with low extinction, since there may be additional obscuration which should not be attributed to the torus. The line of sight to the quasar nucleus could easily suffer a few magnitudes of visual extinction in its passage through the host galaxy, or through foreground companion objects such as those seen in our images of 3C 22. The one-sided radio jet displayed by 3C 22 suggests a smaller angle between the radio (and torus) axis and the line of sight than in 3C 41 and 3C 65, which have similar nuclear extinctions, so it is quite possible that the torus provides only a fraction (if any) of the obscuration. In fact, of the four quasar nuclei we detect at  $L'$ , it is only 3C 265 that we can say with reasonable certainty is seen through the heavy obscuration of the torus.

The fact that we have needed to increase one of the parameters of the receding torus model, namely the torus density  $n_H$ , to allow the model to fit our data, suggests that some refinements are needed. The torus density could increase as a function of redshift, or quasar luminosity (either directly or through the mass of the central black hole or host galaxy), or both. Obviously this question can only be answered by examining the distribution of extinctions in a sample selected at a fainter radio flux limit, such as the 7C sample (selected at a flux level 25 times fainter than LRL; Willott et al. 1998a) although such a study is clearly beyond the capabilities of UKIRT. We can, however, glean something just from the quasar fraction in the 7C sample in the same redshift range, which is consistent with the model's prediction of 11% (Willott et al. 1998a). The relatively small number statistics prevent this from being a definitive test, although the agreement is certainly encouraging and suggests that the torus height might be the same in all sources, irrespective of their redshifts and luminosities.

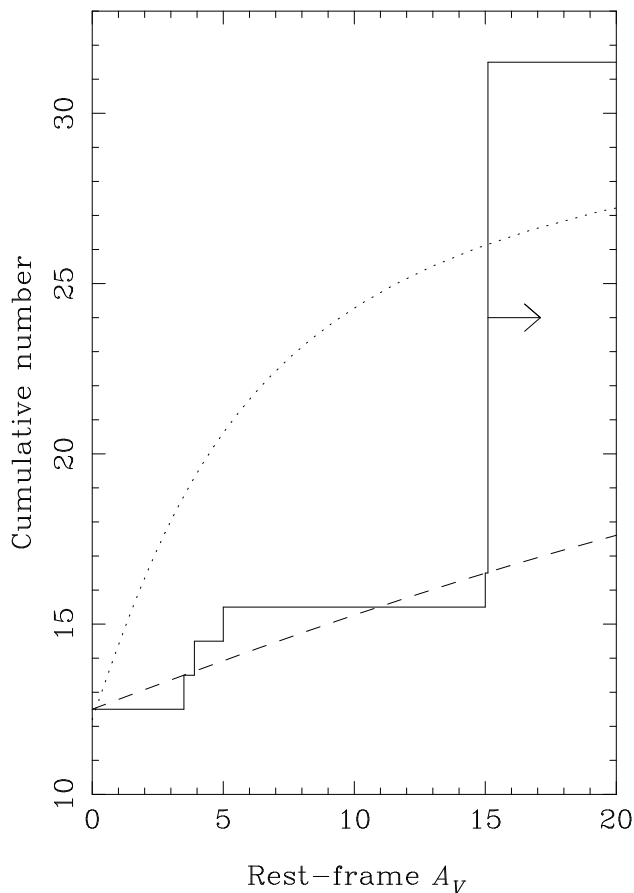


**Figure 12.** Cumulative distribution of nuclear extinction for our sample of radio sources (including the 12.5 ‘virtual’ quasars). The solid line shows the data and the dotted line shows the prediction of the receding torus model of Hill et al. (1996). The dashed line shows the prediction for the receding torus model, renormalized to the statistics of our sample.

## 7 UTILITY OF THE THERMAL IMAGING TECHNIQUE

The sensitivity of thermal imaging observations to point sources is essentially limited by two factors. First, the size of the detection aperture controls the detection threshold, and so the better the image quality achievable, the greater the sensitivity. Secondly, there is effectively a maximum integration time set by the stability of the background from the telescope, and so the rate at which source photons are detected is also important. Obviously then, the diffraction-limited images that the new class of 8-m telescopes should be able to obtain at  $L'$  (FWHM  $< 0''.2$ ) will enable much deeper observations than we have been able to undertake.

The Infrared Camera and Spectrograph (IRCS; Tokunaga et al. 1998) to be installed on the 8.3-m Subaru Telescope in 1999 will be able to achieve a  $3\sigma$  detection of a point source with  $L' = 19.0$  in 1 hour of integration, by using a  $0''.5$  detection aperture. For an intrinsic magnitude of  $L'_0 \approx 13$ , this would allow the detection of the quasar nucleus through as much as  $A_V \approx 50$  mag of obscuration. In reality, the sensitivity will be slightly worse than this due to the presence of the host galaxy which is expected to have

$L' \approx 17$ – $18$  within a  $0''.5$  aperture (assuming  $r_e = 1''.5$  and  $K - L' = 1$ ). However, the excellent image quality should enable the nuclear point source, if present, to be separated from the underlying galaxy with relative ease and so much of the increased sensitivity will be retained.

The ability to measure obscuring columns to this depth would provide a much more rigorous test of the receding torus model than could be presented here. The model shown by the dashed line in Fig. 12 predicts only six sources should be detected with  $15 < A_V < 50$ , while the remaining nine will have even larger obscurations. As was discussed in Section 6.2, it is important not to put too much weight on those sources with low extinction ( $A_V \lesssim 5$ ) since some or even all of this material may come from a source other than the torus. Given the apparent evidence that no property of the torus is constant, the predictive power of the receding torus model rests in its ability to infer the obscuration towards the nuclei which are too heavily obscured to be detected directly.

Improved sensitivity of the thermal-infrared imaging method will also allow studies at much higher redshifts. This is an important extension because there are obvious difficulties with forming enough dust for an  $A_V \sim 50$  torus in an arbitrarily short time, so there is likely to be some critical redshift beyond which all radio sources have low  $A_V$ .

Thermal-infrared imaging may also play an important rôle in understanding the intrinsic orientation dependence of quasar emissions. If the thermal-infrared flux arises from optically-thin material and is isotropic, then statistical studies of, for example, the  $B - L'$  colours of  $z \sim 1$  quasar nuclei could be used to test whether the (rest-frame) UV continuum is also isotropic. Low-frequency selected samples, such as those from the 3C and 7C samples, should contain quasars randomly distributed in orientation with  $\theta \leq \theta_c$ , and would provide a suitable basis for such a study. One possibility would be to look for a correlation between  $B - L'$  colour (corrected for reddening) and radio core dominance. Various studies (e.g., Netzer 1987) have suggested that the UV continua, and the low-ionisation broad emission lines arise in optically-thick disks and thus emit anisotropically.

## 8 SUMMARY

We have presented the results of a near- and thermal-infrared imaging survey of a representative sample of 19  $z \sim 1$  radio galaxies from the 3CR and 3CRR (LRL) samples. Four objects were detected at  $L'$ , with red  $K - L'$  colours which we attributed to partially-obscured quasar light. We have used our infrared data to infer the nuclear extinctions and contributions from non-stellar light at  $K$  for these four sources, and find the results to be in excellent agreement with a more detailed analysis incorporating *HST* data. We deduce that the fraction of dust-reddened quasars at  $z \sim 1$  is  $28^{+25}_{-13}\%$  (90% confidence). We find that the non-stellar light provides as much as 80 per cent of the small-aperture  $K$ -band flux in two objects classified as ‘radio galaxies’, although it is unable to account for the brighter  $K$ -magnitudes of 3C radio galaxies compared to 6C radio galaxies at the same redshift, which must therefore be due to a correlation between radio and host galaxy luminosities. We have also investigated the observed distribution of nuclear

extinctions in our sample in the context of the receding torus model. Although the smaller fraction of lightly-reddened nuclei is in qualitative agreement with the predictions of the model, a quantitative match can only be made by altering one of its parameters. We therefore conclude that the receding torus model has limited predictive power when comparing samples of radio sources at different redshifts and/or radio luminosities, although we have been unable to determine whether it can be applied to a single sample of sources with similar properties. Deeper thermal-infrared imaging, which will be possible in the near future, will be able to answer this and other questions.

## ACKNOWLEDGMENTS

The United Kingdom Infrared Telescope is operated by the Joint Astronomy Centre on behalf of the U. K. Particle Physics and Astronomy Research Council. The authors are grateful to the UKIRT engineers and especially to Tim Carroll, Tim Hawarden and Nick Rees for creating a trouble-free night of observing with the fast guider on its first night of public use. We also wish to thank Katherine Blundell and Chris Willott for taking  $L'$  data on 3C 22, Frossie Economou for communicating the results on the spectra of 3C 41 and 3C 265 in advance of publication, and Neil Medley, Sebastian Jester and Susan Scott for checking the *HST* model fitting. Both Chris Willott and the anonymous referee are thanked for a critical reading of the manuscript which led to substantial improvements. This work is based in part on observations with the NASA/ESA *Hubble Space Telescope*, obtained from the data archive at the Space Telescope Science Institute, which is operated by AURA, Inc. under NASA contract NAS5-26555.

## REFERENCES

- Barthel P. D., 1989, *ApJ*, 336, 606  
 Barvainis R., 1987, *ApJ*, 320, 537  
 Benn C. R., Vigotti M., Carballo R., Gonzalez-Serrano J. I., Sánchez S. F., 1998, *MNRAS*, 295, 451  
 Bennett A. S., 1962a, *MemRAS*, 68, 163  
 Bennett A. S., 1962b, *MNRAS*, 125, 75  
 Best P. N., Longair M. S., Röttgering H. J. A., 1997, *MNRAS*, 292, 758  
 Best P. N., Longair M. S., Röttgering H. J. A., 1998, *MNRAS*, 295, 549  
 Blundell K. M., Rawlings S., Riley J. M., Willott C. J., Laing R. A., 1998, in preparation  
 Bogers W. J., Hes R., Barthel P. D., Zensus J. A., 1994, *A&AS*, 105, 91  
 Bruzual A. G., Charlot S., 1993, *ApJ*, 405, 538  
 Bruzual A. G., Charlot S., 1998, in preparation  
 Chambers K. C., Miley G. K., van Breugel W. J. M., 1987, *Nat*, 329, 604  
 Cimatti A., Dey A., van Breugel W., Antonucci R., Spinrad H., 1996, *ApJ*, 465, 145  
 de Vaucouleurs G., 1948, *Ann. Astrophys.*, 11, 247  
 de Vries W. H., et al., 1997, *ApJS*, 110, 191  
 Dey A., Spinrad H., 1996, *ApJ*, 459, 133  
 Dickson R., Tadhunter C., Shaw M., Clark N., Morganti R., 1995, *MNRAS*, 273, L29  
 Eales S. A., 1985, *MNRAS*, 217, 149  
 Eales S. A., Rawlings S., 1993, *ApJ*, 411, 67  
 Eales S. A., Rawlings S., 1996, *ApJ*, 460, 68  
 Eales S. A., Rawlings S., Dickinson M., Spinrad H., Hill G. J., Lacy M., 1993, *ApJ*, 409, 578  
 Eales S., Rawlings S., Law-Green D., Cotter G., Lacy M., 1997, *MNRAS*, 291, 593  
 Economou F., Lawrence A., Ward M. J., Blanco P. R., 1995, *MNRAS*, 272, L5  
 Economou F., et al., 1998, in preparation  
 Elvis M., et al., 1994, *ApJS*, 95, 1  
 Falcke H., Malkan M. A., Biermann P. L., 1995, *A&A*, 298, 475  
 Francis P. J., Hewett P. C., Flotz C. B., Chaffee F. H., Weymann R. J., Morris S. L., 1991, *ApJ*, 373, 465  
 Hill G. J., Goodrich R. W., DePoy D. L., 1996, *ApJ*, 462, 163  
 Jackson N., Eracleous M., 1995, *MNRAS*, 276, 1049  
 Jackson N., Rawlings S., 1997, *MNRAS*, 286, 241  
 Jannuzi B. T., Elston R., 1991, *ApJ*, 366, L69  
 Kobayashi Y., Sato S., Yamashita T., Shiba B., Takami H., 1993, *ApJ*, 404, 94  
 Kriss G. A., 1994, in Crabtree D. R., Hanisch R. J., Barnes J., eds, *ASP 61: ADASS III*. ASP, San Francisco, p. 437  
 Krist J., 1995, in Shaw R. A., Payne H. E., Hayes J. J. E., eds, *ASP 77: ADASS IV*. ASP, San Francisco, p. 349  
 Lacy M., Rawlings S., 1994, *MNRAS*, 270, 431  
 Lacy M., Rawlings S., Eales S., Dunlop J. S., 1995, *MNRAS*, 273, 821  
 Laing R. A., Riley J. M., Longair M. S., 1983, *MNRAS*, 204, 151  
 Lawrence A., 1991, *MNRAS*, 252, 586  
 Leyshon G., Eales S. A., 1998, *MNRAS*, 295, 10  
 Lilly S. J., 1989, *ApJ*, 340, 77  
 Lilly S. J., Longair M. S., 1982, *MNRAS*, 199, 1053  
 Lilly S. J., Longair M. S., 1984, *MNRAS*, 211, 833  
 Lilly S. J., Longair M. S., Miller L., 1985, *MNRAS*, 214, 109  
 Longair M. S., 1975, *MNRAS*, 173, 309  
 McCarthy P. J., 1988, Ph.D. thesis, Univ. California Berkeley  
 McCarthy P. J., 1993, *ARA&A*, 31, 639  
 McCarthy P. J., Miley G. K., de Koff S., Baum S. A., Sparks W. B., Golombek D., Biretta J., Macchetto F., 1997, *ApJS*, 112, 415  
 McCarthy P. J., van Breugel W. J. M., Spinrad H., Djorgovski S., 1987, *ApJ*, 321, L29  
 McGlynn T., Scollick K., White N., 1996, in McLean B. J. et al., eds *IAU 179: New Horizons from Multi-Wavelength Sky Surveys*. Kluwer, Dordrecht, p. 465  
 Netzer H., 1987, *MNRAS*, 225, 55  
 Neugebauer G., Green R. F., Matthews K., Schmidt M., Soifer B. T., Bennett J., 1987, *ApJS*, 63, 615  
 Owen F. N., Puschell J. J., 1984, *AJ*, 89, 932  
 Pei, Y.C., 1992, *ApJ*, 395, 130  
 Rawlings S., Saunders R., 1991, *Nat*, 349, 138  
 Rawlings S., Lacy M., Sivia D. S., Eales S. A., 1995, *MNRAS*, 274, 428  
 Rawlings S., Blundell K. M., Lacy M., Willott C. J., Eales S. A., 1998a, in Bremer M. N., Jackson N., Pérez-Fournon I., eds *Observational Cosmology with the New Radio Surveys*. Kluwer, Dordrecht, p. 171  
 Rawlings S., et al., 1998b, in preparation  
 Rhee G., Marvel K., Wilson T., Roland J., Bremer M., Jackson N., Webb J., 1996, *ApJS*, 107, 175  
 Rigler M. A., Lilly S. J., 1994, *ApJ*, 427, L79  
 Roche N., Eales S., Rawlings S., 1998, *MNRAS*, 297, 405  
 Rowan-Robinson M., Hughes J., Jones M., Leech K., Veda K., Walker D. W., 1991, *MNRAS*, 249, 729  
 Sanders D. B., Phinney E. S., Neugebauer G., Soifer B. T., Matthews K., 1989, *ApJ*, 347, 29  
 Scheuer P. A. G., 1987, in Pearson T. J., Zensus J. A., eds, *Superluminal Radio Sources*. CUP, Cambridge, p. 104  
 Serjeant S., Rawlings S., 1996, *Nat*, 379, 304



- Serjeant S., Rawlings S., Maddox S. J., Baker J. C., Clements D.,  
Lacy M., Lilje P. B., 1998, MNRAS, 294, 494  
Simpson C., 1998, MNRAS, 297, L39  
Smith H. E., Spinrad H., 1980, ApJ, 236, 419  
Stockton A., Kellogg M., Ridgway S. E., 1995, ApJ, 443, L96  
Stockton A., Ridgway S. E., Kellogg M., 1996, AJ, 112, 902  
Strom R. G., Riley J. M., Spinrad H., van Breugel W. J. M.,  
Djorgovski S., Liebert J., McCarthy P. J., 1990, A&A, 227,  
19  
Tadhunter C. N., Scarrott S. M., Draper P., Rolph C., 1992, MN-  
RAS, 256, 53P  
Tokunaga, A. T., et al., 1998, in SPIE 3354: Infrared Astronomical  
Instrumentation, ed. A. M. Fowler, 512  
Tran, H. D., Cohen, M. H., Ogle, P. M., Goodrich, R. W., di  
Serego Alighieri, S., 1998, ApJ, 500, 660  
Webster R. L., Francis P. J., Peterson B. A., Drinkwater M. J.,  
Masci F. J., 1995, Nat, 375, 469  
Willott, C. J., Rawlings, S., Blundell, K.M., Lacy, M., 1998a, M.  
N. Bremer et al., eds Observational Cosmology with the New  
Radio Surveys. Kluwer, Dordrecht, p. 209  
Willott, C. J., Rawlings, S., Blundell, K. M., Lacy, M., 1998b,  
MNRAS, 300, 625  
Willott, C. J., Rawlings, S., Blundell, K. M., Lacy, M., 1998c,  
MNRAS, in press